Published in final edited form as:
Nature. 2022 June ; 606(7916): 930–936. doi:10.1038/s41586-022-04767-1.

Breakage of cytoplasmic chromosomes by pathological DNA base excision repair

Shangming Tang[1,2,3], **Ema Stokasimov**[1,2,3], **Yuxiang Cui**[4], **David Pellman**[1,2,3,+]

[1]Howard Hughes Medical Institute, Chevy Chase, MD 20815, USA.

[2]Department of Pediatric Oncology, Dana-Farber Cancer Institute, Boston, MA 02215, USA.

[3]Department of Cell Biology, Blavatnik Institute, Harvard Medical School, Boston, MA 02215, USA.

[4]Department of Chemistry, University of California, Riverside, Riverside, CA, 92521, USA.

Abstract

Chromothripsis is a catastrophic mutational process that promotes tumorigenesis and causes congenital disease[1–4]. Chromothripsis originates from aberrations of nuclei called micronuclei or chromosome bridges[5–8]. These structures have fragile nuclear envelopes (NEs) that spontaneously rupture[9,10], leading to DNA damage when chromatin is exposed to the interphase cytoplasm. Here, we identify a mechanism explaining a major fraction of this DNA damage. Micronuclei accumulate large amounts of RNA-DNA hybrids, which are edited by ADAR enzymes (adenine deaminases acting on RNA) to generate deoxyinosine (dI). dI is then converted into abasic sites by a DNA base excision repair (BER) glycosylase, MPG (N-methyl-purine DNA glycosylase)[11,12]. These abasic sites are cleaved by the BER endonuclease, APE1 (apurinic/apyrimidinic endonuclease)[12], creating single-strand DNA nicks that can be converted to DNA double strand breaks by DNA replication or when closely spaced nicks occur on opposite strands[13,14]. This model predicts that MPG should be able to remove the dI base, hypoxanthine, from the DNA strand of RNA-DNA hybrids, which we demonstrate using pure proteins and oligonucleotide substrates. These findings identify a mechanism for fragmentation of micronuclear chromosomes, an important step in generating chromothripsis. Rather than breaking any normal chromosome, we propose that the eukaryotic cytoplasm only damages chromosomes with preexisting defects such as the DNA base abnormality described here.

Chromothripsis involves extensive, localized chromosome rearrangement with a characteristic DNA copy number pattern[3]. It is common in cancer, where it accounts for a substantial fraction of genome rearrangements[15]. Chromothripsis causes tumor suppressor loss, oncogenic translocations, and oncogene amplification via the formation

---

[+] Correspondence should be addressed to: David Pellman, Dana-Farber Cancer Institute, 44 Binney St., Rm. M663, Boston, MA 02115, Phone: (617) 312-0098, Fax: (617) 632-6845, David_Pellman@dfci.harvard.edu.

Author Contributions

D.P. and S.T. designed the experiments. D.P. and S.T. wrote the manuscript, with edits from all authors. S.T. performed most experiments. Y.C. contributed preliminary data.

Competing interest

D. Pellman is a member of the Volastra Therapeutics SAB.

of extrachromosomal circular DNA[3,5,7,16]. It also causes developmental defects in organisms as disparate as plants and humans[17–19]; it can be passed through the germline, and therefore in principle, it could contribute to karyotype changes during organismal evolution. Understanding the mechanism of chromosome fragmentation underlying chromothripsis is therefore central to understanding genome evolution in many contexts.

Chromothripsis is generated during a single cell division by a cascade of DNA damage initiated by the formation of micronuclei (MN)[5,20] or chromosome bridges[6,8]. A major fraction of DNA damage occurs in interphase, when the nuclear envelope (NE) of the MN ruptures, exposing the enclosed chromosome(s) to the cytoplasm[9]. A second wave of damage occurs when cells with MN chromosomes enter mitosis, at which point the MN chromosome undergoes a burst of aberrant DNA replication[8]. Ligation of the resulting DNA fragments in random order and orientation generates chromothripsis.

Pathological BER in micronuclei

Among several possibilities, we tested the hypothesis that DNA damage in ruptured MN results from aberrant DNA base excision repair (BER) involving the APE1 endonuclease (also known as APEX1). To generate cells with MN, we synchronized p53-deficient cells in the G2 phase with a cyclin-dependent kinase (CDK1) inhibitor and released them in the presence of an inhibitor of the MPS1 spindle assembly checkpoint kinase to cause chromosome missegregation and micronucleation (Fig. 1a)[10]. Because the majority of DNA damage to interphase MN occurs after NE rupture in cells that have entered S phase (Extended Data Fig. 1a, b)[5,9], we assessed the amount of DNA damage (γ-H2AX or TUNEL-labeling) in EdU labeled cells that had undergone NE rupture. This cell cycle synchronization procedure enabled us to determine the genetic requirements for the DNA damage in ruptured interphase MN, independent of mitotic DNA damage[8].

We constructed homozygous null *APE1* RPE-1 cell lines to determine if APE1 is required for MN DNA damage (Extended Data Fig. 1c, d). Two independent clones lacking APE1 exhibited more than 2-fold reduction in interphase MN DNA damage, assessed by γ-H2AX labeling (Extended Data Fig. 1d). Similar results were obtained with genome-edited U2OS cells (Extended Data Fig. 1e). To avert potential preexisting DNA damage or adaptation to APE1 loss, we also generated lines where APE1 destruction could be conditionally induced[21]. Both endogenous alleles of *APE1* were modified to contain the coding sequence for two tandem degrons, enabling near-complete APE1 degradation within ~ 60 minutes (Fig. 1b). In synchronized cells, acute loss of APE1 led to a ~3 to 4-fold reduction in MN DNA damage, assessed either by γ-H2AX-labeling or the TUNEL assay (Fig. 1c–e and Extended Data Fig. 1f, g). Similar results were also observed after APE1 was degraded in unsynchronized cells (Extended Data Fig. 2a–c). APE1 endonuclease activity is required to generate MN DNA damage because a catalytically inactive APE1 variant[22] failed to complement APE1-deficient cells (Fig. 1f, g and Extended Data Fig. 2d, e). Although wild-type APE1 did not accumulate on ruptured MN, a catalytically inactive APE1 mutant with a slow off-rate did (Fig. 1h, i) [22]. Together, these data indicate that a large fraction of interphase DNA damage in ruptured MN is mediated by APE1. Although the immediate effect of APE1 is to generate ssDNA nicks, these nicks can be converted into dsDNA breaks by DNA replication through the nick or when adjacent nicks on both DNA strands are generated, as occurs during immunoglobulin class switch recombination[13,14].

During base excision repair, APE1 cleaves abasic sites generated by one of 11 human DNA glycosylases[12]. We used RNA interference in synchronized cells to identify glycosylases required for MN DNA damage (Fig. 2a). For 10 out of the 11 glycosylases, available antibody reagents enabled us to verify the extent of siRNA-mediated knockdown (Extended Data Fig. 3a). Knockdown of only one glycosylase, the N-methylpurine DNA glycosylase[11] (hereafter MPG, also known as the 3-alkyladenine DNA glycosylase or AAG) attenuated DNA damage in ruptured MN (Fig. 2a). Unlike APE1, wild-type MPG accumulated heavily on ruptured MN in the cytoplasm, as shown by gene disruption-validated antibodies to detect the endogenous protein, or by exogenous expression of an epitope-tagged MPG variant (Fig. 2b and Extended Data Fig. 3b). The requirement for MPG in MN DNA damage was confirmed in two null-allele cell lines (RPE-1 and U2OS, Extended Data Fig. 4a–d) and with cell lines expressing MPG with tandem-conditional degrons (RPE-1, Fig. 2c–f). Moreover, MPG's ability to trigger MN DNA damage requires its catalytic activity[23] (Fig. 2g and Extended Data Fig. 4b). Because the effects of MPG loss and APE1 loss are comparable, MPG appears to be the primary glycosylase in this pathway.

If BER generates MN DNA breaks, why are APE1-generated ssDNA nicks not repaired? We considered the possibility that this is explained by the loss of downstream BER repair factors upon rupture of the MN NE. Indeed, multiple factors required for the repair of BER-derived ssDNA nicks were lost from ruptured MN (Extended Data Fig. 5).

Abnormal DNA base content of micronuclei

MPG acts on a broad range of substrates including alkylated bases, base adducts generated by lipid peroxidation, and hypoxanthine, a normal intermediate in purine biosynthesis[11]. Because MPG has the highest activity for hypoxanthine[11], which in RNA is inosine (I) and in DNA is deoxyinosine (dI), we determined if MN chromosomes contain increased amounts of dI.

We used sequential sucrose gradient fractionation to separate MN from the primary nuclei (PN, Fig. 3a)[24]. Using an oligonucleotide-validated α-inosine dot blot assay (Extended Data Fig. 6a), we tested this hypothesis but found comparable α-inosine labeling in MN and PN fractions isolated from wild-type cells. However, there was an ~12-fold enrichment of the α-inosine signal if the MN fraction was isolated from cells lacking MPG (Fig. 3b and Extended Data Fig. 6b). Similarly, when cells were stained with the α-inosine antibody, we observed ~5-fold enriched labeling of MN in *MPG* null cells but not in *MPG* wild-type cells (Fig. 3c, d and Extended Data Fig. 6c). The specificity of the α-inosine signal for MN in cells lacking the MPG DNA glycosylase and its resistance to digestion with multiple RNases (RNase A, RNase H1, and RNase III, see Methods) suggest that MPG removes hypoxanthine bases from MN DNA in wild-type cells. Therefore, MN chromosomes appear to accumulate dI, leading to processing by MPG and APE1 to generate ssDNA breaks.

ADARs process MN RNA-DNA hybrids

There are two potential ways for dI to become incorporated into DNA. DNA polymerases can misincorporate dI if it is present at abnormally high levels in nucleoside pools[25,26]. Although we cannot exclude this possibility, overexpression of inosine triphosphate pyrophosphatase (ITPA), the enzyme which purges I and dI from nucleoside pools, did not reduce MN DNA damage (Extended Data Fig. 6d, e). dI could also be generated by deamination of adenine, but there is no natural enzyme known to deaminate adenine in double stranded DNA (dsDNA) in eukaryotic cells[27]. However, it was recently determined that dI can be generated on the DNA strand of RNA-DNA hybrids by ADAR deaminases that normally act on double stranded RNA (dsRNA)--albeit with reduced catalytic efficiency[28]. Despite clear in vitro evidence for ADAR activity on RNA-DNA hybrids, cellular contexts where this activity is relevant are only starting to be identified[29,30].

We determined if MN accumulate RNA-DNA hybrids. We probed MN and PN DNA fractions using a dot blot assay with the S9.6 antibody to detect RNA-DNA hybrids. In wild-type cells the MN fraction exhibited heavy enrichment of S9.6-labeling relative to the signal in the PN fraction (Fig. 3e and Extended Data Fig. 6f). Unexpectedly, this MN fraction S9.6 signal was further enriched ~3-fold when MN and PN were prepared from $MPG^{-/-}$ cells (Fig. 3f), suggesting that MPG breakage of DNA strands may inhibit the accumulation of MN-associated RNA-DNA hybrids.

The following evidence indicates that the S9.6 signal from MN fractions reflects bone fide RNA-DNA hybrids: (1) almost all of the S9.6 signal was eliminated by treatment of the MN fraction with RNase H, which digests RNA-DNA hybrids[31], however, it is not eliminated by RNase A treatment, which digests single stranded RNA (Fig. 3e); (2) the residual S9.6 signal after RNase H treatment was abolished by RNase III treatment, which digests dsRNA known to be weakly detected by S9.6 (Fig. 3e) [32]; (3), overexpression of RNase H1, which degrades RNA-DNA hybrids, or overexpression of the catalytic domain of the Senataxin helicase, which unwinds them[33], both reduced MN DNA damage (3-fold and 2-fold respectively, Fig. 3g and Extended Data Fig. 6g–m); (4), catalytically inactive RNase H1 (RNaseH1-CI), which binds RNA-DNA hybrids in vivo[34], accumulated on ruptured MN in cells lacking MPG (Extended Data Fig. 7a, b). Therefore RNA-DNA hybrids accumulate on MN chromosomes where they promote DNA damage.

One mechanism that could explain hybrid generation on MN chromosomes would be the trapping of nascent transcripts on their DNA template when the MN NE breaks and transcription abruptly stops[9]. Another, non-exclusive possibility is that some hybrids form even before MN rupture, because of the nuclear transport defects of MN that might impair the accumulation of proteins required for normal hybrid processing[10]. Supporting a role for transcription, treatment of synchronized micronucleated cells with a high dose of the transcription inhibitor 5,6-dichloro-1-beta-D-ribofuranosylbenzimidazole (DRB) reduced MN DNA damage 7-fold (Extended Data Fig. 7c, d). This is not solely due to DRB-induced cell cycle arrest in G1, because treatment of cells with a lower concentration of DRB, which allows some cells to progress into S phase, also reduced MN DNA damage in these S phase cells (Fig. 3h and Extended Data Fig. 7e, f). Furthermore, inhibition of transcription with

DRB caused a reduction in the recruitment of MPG to ruptured MN without affecting MN rupture frequency, supporting the model that transcription-generated hybrids become MPG substrates (Extended Data Fig. 7g–h).

We generated cells lacking ADARs to determine if these enzymes are required for MN DNA damage. The loss of ADAR function is lethal in RPE-1 cells, presumably because of spurious activation of innate immune signaling. We therefore generated ADAR1 and ADAR2 single and double mutant null RPE-1 cells lacking the innate immune sensor, melanoma differentiation-associated protein 5 (MDA5)[35]. Loss of either ADAR1 or ADAR2 partially suppressed MN DNA damage and cells lacking both enzymes reduced DNA damage to the levels comparable with the loss of MPG or APE1 (Fig. 3i and Extended Data Fig. 8a–g, RPE-1 and U2OS cells). The absence of MDA5 does not affect these results because RNAi-mediated suppression of ADAR1 and ADAR2 in MDA5-proficient cells also reduced MN DNA damage (Extended Data Fig. 8h, i).

Complementation experiments with one of the two major *ADAR1* splice isoforms, p150, or a catalytically inactive derivative[35], demonstrated that ADAR deaminase activity is required to generate MN DNA damage (Fig. 3i and Extended Data Fig. 9a–c). By contrast, expression of ADAR2 or the ADAR1 p110 isoform only partially complimented *ADAR1 ADAR2* null cells (Fig. 3i and Extended Data Fig. 9c). Inefficient complementation by ADAR2, and probably p110, is likely due to the nuclear localization of ADAR2 and ADAR1 p110, which sequesters them from cytoplasmic MN chromosomes. In support of this conclusion, the expression of a cytoplasmic ADAR2 variant lacking its nuclear localization signal fully complemented *ADAR1 ADAR2* double deletions (Extended Data Fig. 9c, d). Also supporting the conclusion that ADARs act on RNA-DNA hybrids to generate dI, overexpression of RNase H1 or the loss of ADAR1 and ADAR2 attenuated the α-inosine immunofluorescence signal on MN chromosomes in cells lacking MPG (Extended Data Fig. 9e–h, Extended Data Fig. 10 a, b).

These results suggest the following model (Fig. 4a). RNA-DNA hybrids accumulate on MN chromosomes; after hybrids form, ADAR-mediated editing generates dI that is then converted to ssDNA nicks by the combined action of MPG and APE1. This model makes a strong biochemical prediction: MPG should have the ability to remove the hypoxanthine base from the DNA strand of an RNA-DNA hybrid.

MPG acts on RNA-DNA hybrids

We tested this hypothesis using pure proteins and oligonucleotide substrates. dsDNA, dsRNA, or RNA-DNA hybrid substrates were generated with a 5’ fluorescent label on one strand of each double-stranded oligonucleotide (Fig. 4b left panel) [36]. The synthesized substrates contained either I or dI at a defined position on the labeled strand (opposite a U or dT residue on the unlabeled strand). Control substrates lacking I or dI were also synthesized. To assay for MPG-mediated hypoxanthine base removal, these oligonucleotide substrates were exposed to MPG for varying time intervals followed by a short incubation with APE1. A 15-nucleotide fluorescent cleavage product is produced if MPG and APE1 generate ssDNA nicks at the I or dI residues.

Consistent with our model, we observed robust MPG activity on dI in the DNA strand of RNA-DNA hybrids (Fig. 4b right panel), an activity that was only moderately lower than that observed on dI in dsDNA. We did not observe any activity of MPG towards RNA, either in the context of dsRNA or RNA-DNA hybrids (Fig. 4b right panel). The absence of detectable cleavage products using control substrates lacking I or dI confirmed the specificity of these results for the hypoxanthine base (Extended Data Fig. 10c). To assay MPG activity independently of APE1 cleavage at abasic sites in DNA or RNA [36], we used the α-inosine dot blot assay, which confirmed the ability of MPG to remove the hypoxanthine base from the DNA strand of an RNA-DNA hybrid (Fig. 4c).

Discussion.

We demonstrate that pathological BER makes a major contribution to the DNA fragmentation of MN chromosomes, a central step in the mechanism of chromothripsis[1,5,8]. Aberrant BER is triggered by heavy accumulation of RNA-DNA hybrids in MN, providing a substrate that enables ADAR enzymes to modify DNA. This ultimately leads to unrepaired DNA nicks, because of the loss of downstream BER nick-repair factors after MN NE rupture (Extended Data Fig. 5). A prior study showed that ADAR enzymes can edit the DNA strand of RNA-DNA hybrids in vitro[28]; the findings described here identify an important biological context for this activity. Validating a central feature of our model, we show that MPG has the ability to remove hypoxanthine bases from the DNA strand of RNA-DNA hybrids.

These results raise the question of whether ADAR-mediated DNA editing would leave mutational scars in cancer genomes. This would not necessarily be the case because MPG, which is widely expressed in tumors, will remove dI and mask A>G transitions, as we found in our experiments (Fig. 3b–d; Extended Data Fig. 6b, c; Extended Data Fig. 9e–h; Fig. 4b, c). Nevertheless, ADAR editing might generate mutational scars in certain circumstances: ADAR enzymes can be overexpressed in tumors[37] and engineered mice with high-level overexpression of ADAR1 show an increased frequency of A>G transitions at loci prone to R-Loop formation that are also enriched for the ADAR target consensus sequence[38–40]. Moreover, there are unexplained cancer mutation signatures that include A>G mutations[41].

In addition to pathological BER, other mechanisms likely contribute to the fragmentation of MN chromosomes. This is implied by the residual interphase DNA damage we observe after the loss of MPG or APE1. Several candidates for additional DNA breakage mechanisms have been proposed (Supplementary Information)[42–45]. Furthermore, MN chromosomes undergo a second round of DNA damage during a burst of DNA replication that occurs when micronucleated cells enter mitosis[8]. Multiple damage mechanisms likely explain why chromothripsis breakpoints are distributed relatively evenly across the genome[3,4].

Finally, the DNA breakage process described here might be pathological, only occurring when MN chromosomes are exposed to the cytoplasm. Alternatively, because MPG suppresses hybrid formation on ruptured MN ~3-fold (Fig. 3f), MPG could have a yet-to-be identified, physiological role in the processing of RNA-DNA hybrids.

Methods:

Cell culture.

Telomerase-immortalized RPE-1 and U2OS cells were from ATCC. RPE-1 derived cell lines were grown in phenol red-free DMEM: F12 medium (Gibco, cat #: 21041–025) containing 10% FBS (GeminiBio, BenchMark™ Cat #: 100–106), 100 IU mL^{-1} penicillin and 100μg mL^{-1} streptomycin (Gibco, cat #: 15140–122). U2OS derived cell lines were maintained in DMEM+GlutaMAX™ (Gibco, cat #:10569–010) with the same antibiotics and FBS as for RPE-1 cells. Note: for all cell lines with doxycycline-induced construct expression, we used doxycycline-free FBS (CPS serum, cat #: FBS-500). Cells were cultured at 37°C with 5% CO_2 atmosphere with 100% humidity. For cell cycle synchronization and MN induction, cells were seeded to 12-well plates 12 hours prior to addition of 9 μM of the CDK1 inhibitor, RO3306 (MilliporeSigma™, cat #: 217699–5MG). RO3306 was then added for 18 hours. Cells were washed five times with fresh medium containing 10% FBS and then cultured in medium with 1 μM NMS-P715 (MPS1 inhibitor, MilliporeSigma™, cat #: 475949–5MG). EdU (10 μM) was added to cultures 2 hours after RO3306 washout. For induced degradation of AID-SMASh-tagged proteins, doxycycline (2 μg/mL), IAA (500 μM, Santa Cruz Biotechnology, cat #: sc-215171) and Asunaprevir (3 μM, Cayman chemical, cat #:20835) were added with RO3306 and these drugs were maintained in the culture medium after RO3306 washout. For overexpression of RNaseH1 or C-Senataxin, doxycycline (2 μg/mL) was added with RO3306 and then maintained in the medium after RO3306 washout.

RNA interference.

Cells at 50% confluency were transfected with 40nm siRNA using Lipofectamine 3000 (Life Technologies, cat #: L3000015) according to the manufacturer’s instructions. Transfections were performed 24 hours before cell cycle synchronization with RO3306. The following siRNAs were used in this study: ON-TARGETplus Non-targeting Pool (Horizondiscovery, cat #: D-001810–10-20) as a control; Human TP53 siRNA-SMARTpool (Horizondiscovery, cat #: L-003329–00-0020); Human MPG ON-TARGETplus siRNA SMARTpool (Horizondiscovery, cat #: L-005146–00-0020); Human UNG ON-TARGETplus siRNA SMARTpool (Horizondiscovery, cat #: L-011795–00-0005); Human SMUG1 ON-TARGETplus siRNA SMARTpool (Horizondiscovery, cat #: L-012838–01-0010); Human NEIL1 ON-TARGETplus siRNA SMARTpool (Horizondiscovery, cat #: L-008327–00-0005); Human NEIL2 ON-TARGETplus siRNA SMARTpool (Horizondiscovery, cat #: L-016345–01-0005); Human NEIL3 ON-TARGETplus siRNA SMARTpool (Horizondiscovery, cat #: L-020939–01-0010); Human OGG1 ON-TARGETplus siRNA SMARTpool (Horizondiscovery, cat #: L-005147–00-0010); Human MUTYH ON-TARGETplus siRNA SMARTpool (Horizondiscovery, cat #: L-012806–00-0005); Human NTHL1 ON-TARGETplus siRNA SMARTpool (Horizondiscovery, cat #: L-009345–00-0005); Human MBD4 ON-TARGETplus siRNA SMARTpool (Horizondiscovery, cat #: L-011554–00-0005); Human TDG ON-TARGETplus siRNA SMARTpool (Horizondiscovery, cat #: L-003780–01-0005). ADAR2 siRNA: Life Technologies, s1010: CCUGGUCCUGGGUAAGUUUtt; s1012: GCAGAAAUAAUAUCUCGGAtt.

DNA constructs.

cDNAs with *APE1* and *MPG* as well as the Gateway Lenti Vector pHAGE-N-FLAG-HA were gifts from Dr. Wade Harper. cDNA with *ADAR1*, *ADAR2*, *RNASEH1*, *ITPA*, *C-SETX* (Δ1–1850) were from Horizondiscovery. pCW57.1 (plix401, #41393) and plix403 (#41395) were from Addgene. For inducible constructs to express *APE1* and mutants (*APE1-CI*: H309N; *APE1-SO*: D283A, D308A), *RNASEH1* (and CI mutant) *and C-SETX*, cDNAs were PCR amplified, inserted into the pENTR/D-TOPO vector (ThermoFisher, cat #: k240020) and then gateway cloned into destination vectors (plix401 or plix403) was performed. PCR primers were:

APE1: forward 5’ CACCATGCCGAAGCGTGGGAAAAAGGGA 3’; reverse 5’ TCACAGTGCTAGGTATAGGGTGAT 3’. RNASEH1: forward 5’ CACCATGAGCTGGCTTCTGTTCCTGG 3’; reverse 5’GTCTTCCGATTGTTTAGCTCC 3’. C-SEXT: forward 5’ CACCATGGTATTGAATACTTTTGAAACAG 3’; reverse 5’TAAAAGCTTTCTTTTCTTGGAAC3’.

CRISPR-Cas9 gene knockout and gene editing.

Gene disruption null alleles (referred to as “knockouts” if no protein could be detected by western blotting) were generated by CRISPR-Cas9. TrueCut Cas9 v2 (Invitrogen, cat #A36498) was incubated with TrueGuide modified synthetic sgRNA (Thermo Fisher) and RNP transfection was performed using Lipofectamine CRISPRMAX (Invitrogen, cat #: CMAX00008). To create gene fusions with the AID-SMASh coding sequence, a plasmid containing AID-SMASh-NeoR flanked with 500bp homolog arms was transfected with the Cas9 RNPs, providing a template for homology-directed repair. Editing was performed in an RPE-1 cell line with a doxycycline-inducible E3 ligase OsTIR1 transgene at the *ROSA26* locus[21]. 48 hours after transfection, the cells were washed with fresh medium and allowed to recover for one or two days prior to drug selection and single cell sorting. The following guide RNAs were used in this study for knockout. *MPG*: g1 5’ CUAGUCCGGCGACUUCCUAA 3’; g2: 5’ GUUGGAGUUCUUCGACCAGC 3’; *APE1*: g1: 5’ UCAAUACUGGUCAGCUCCUU3’; g2: 5’ AUGCCGAAGCGUGGGAAAAA. *MDA5*: g1: CGAAUUCCCGAGUCCAACCA; g2: AGCGUUCUCAAACGAUGGAG. *ADAR1*: g1: 5’ GUGCAUACACUCAAGCAGUG 3’; g2: 5’ AGAUAGCCAUGCUGAGCCAC 3’; *ADAR2*: g1: 5’ UGUGAAGGAAAACCGCAAUC 3’; g2: 5’ UCUGGACAACGUGUCCCCCA 3’.

Antibodies used in this study:

A 1:100 dilution of primary antibodies was used for immunofluorescence (IF) unless otherwise specified. A 1:1000 dilution of primary antibodies was used for western blots unless otherwise specified. A 1:1000 dilution of secondary antibodies was used for IF and a 1:5000 dilution was used for western blotting. Primary antibodies were used to detect the following proteins: H2A.X (Ser139): clone JBW301 Millipore, (cat #: 05–636-I, 1:500 for IF); H2A.X: Cell Signaling (cat #: 2577 1:500 for IF); BrdU: Abcam (cat #: ab8039); Neil1: Proteintech (cat #: 12145-I-AP 1:500 for western blot); Neil2: Invitrogen (cat #: PA5–78662) or Human Protein Atlas (cat #: HPA073916); NTHL1: Invitrogen (cat #: PA1–32336) or Proteintech (cat #: 14918-I-AP); SMUG1: Abcam (cat

#: ab192240); MPG: Abcam (cat #: ab196553); MBD4: Abcam (cat #: ab224809); TDG: Abcam (cat #: ab154192); MUYTH: Novus Biologicals (cat #: H00004595-M01) 1:500 for western blot; UNG: Thermo Fisher Scientific UNG Monoclonal Antibody OTI1A11 (cat #: MA525680); OGG1: Abcam anti-Ogg1 antibody(cat #: ab62826); ADAR1: Cell Signaling (cat #: 14175S); ADAR2 (ADARB1): Proteintech (cat #: 22248–1-AP at 1:500 for western blot) or Thermofisher (cat #: PA5–36179); V5-tag: Cell Signaling clone D3H8Q (cat #: 13202S) or Abcam (cat #: ab27671); HA-tag: Biolegend clone 16B12 (cat #: 901502); APE1: Abcam (cat # ab137708); BAF(BANF1): Abnova (cat #: 100008815); BAF(BANF1): Abcam (cat #: ab129184); XRCC1: Cell Signaling (Cat #: 2735S; XRCC1: Abcam (cat #: ab134056); DNA polymerase beta: Abcam (cat #:ab175197); LIG1: Abcam (cat #: ab177946); LIGIII: Abcam (cat #: ab185815); LBR: Abcam (cat #: ab32535) or Sigma-Aldrich (cat #: SAB1400151); GAPDH: Abcam (cat #: ab8245) or Abcam (cat #: ab9485); MDA5: Cell Signaling (cat #: 5321S); Inosine: MBL international (cat #: PM098); S9.6 Kerafast (cat #: ENH001); and dsDNA: Abcam (cat #: ab27156).

Secondary antibodies for IF: Life Technologies anti-mouse Alex Fluor 488 (cat #: A11029); Life Technologies anti-rabbit Alex Fluor 488 (cat #: A11034); Life Technologies anti-mouse Alex Fluor 568 (cat #: A11031); and Life Technologies anti-rabbit Alex Fluor 568 (cat #: A11036.) Secondary antibodies for western blots: LI-COR IRDye 800CW anti-mouse (cat #: 92632212,); LI-COR anti-rabbit (cat #: 926–32212); IRDye 680RD LI-COR anti-mouse (cat #: 926–68072); and LI-COR anti-rabbit (cat #: 926–68073).

Indirect immunofluorescence microscopy.

Cells were washed with PBS and fixed with 4% paraformaldehyde for 20 minutes at room temperature. Cells were then washed with PBS three times prior to extraction with 0.5% Triton X-100 in PBS for 15 minutes. Cells were washed with PBS three times and then blocked with 3% BSA in PBS for 1 hour. After blocking, detection of EdU was performed with the Click-iT Plus EdU Alexa Fluor 647 Imaging Kit (Invitrogen, cat #: C10640). Cells were washed two times with PBS, followed by a 1 hour incubation with primary antibodies at room temperature, followed by an overnight incubation at 4°C. Cells were washed three times with 0.05% Triton X-100 in PBS. Species-specific secondary antibodies were added to the cells for 1 hour followed by three washes with 0.05% Triton X-100 in PBS. 2.5 μg/mL Hoechst 33342 in PBS was added to the cells for 10 minutes. After three washes with PBS, Prolong Diamond Antifade (Life Technologies, cat #: P36961) was used for mounting of the samples.

For inosine staining, to degrade RNA, cells were treated with RNase T1 (1:200, 1000 U/μL Life Technologies, cat #: EN0541), RNaseH (1:200, 60 U/μL, Takara, cat #: 2150B) and Shortcut RNase III (1:200, 2 U/μL, NEB, cat #: M0245L) in TBST with 0.1% BSA, 0.1% NaN_3, 3 nM $MgCl_2$ for 6 hours at 37°C[32] after blocking with 3% BSA. The samples were denatured with 4 M HCl for 1 hour at 37°C followed by 3 washes with 0.1 M of Tris-HCl pH8.0[46]. After the denaturing step, EdU detection and primary antibodies (anti-inosine and nuclear ruptured marker anti-BAF) were added to samples for an overnight incubation at 4 °C. IF was then performed as described above.

TUNEL assay.

We performed this assay according to the manufacturer’s instructions with the following modifications [APO-BRDU (TUNEL) Apoptosis Kit, cat #: AU1001]. Cells grown on coverslips were washed with PBS and fixed with 2% paraformaldehyde (PFA) for 20 minutes at room temperature. Cells then were washed with PBS three times prior to extraction with 0.5% Triton X-100 in PBS for 30 minutes. Cells then were washed with PBS three times followed by two washes with Wash buffer from the kit. Then cells were incubated with the DNA labeling solution (50 μL for each coverslip) for four hours at 37°C in a humidity chamber. Cells were washed with Rinse buffer three times at 10 minutes intervals. After the DNA end-labeling, all the following steps were carried out as described for IF staining described above to detect BrdU. We note that the assay is particularly sensitive to the fixation conditions and to the labeling reaction time. Fixation in 1% PFA resulted in uniformly high background whereas fixation in 4% PFA resulted in a near-complete loss of signal. The four hour-labeling (as opposed to the suggested one hour-labeling) strongly enhanced signal detection.

Microscopy.

Imaging was performed on a spinning disk confocal microscope (Nikon Ti-E with a Yokogawa CSU-22 confocal head with the Borealis modification). Z-stacks of nine images at 0.5-μm spacing were collected using a CoolSnap HQ2 CCD camera (Photometrics) or a Prime BSI back-thinned sCMOS camera (Photometrics), with a 60×/1.40 NA or a 100×/1.45 NA Plan Apochromat oil immersion objective (Nikon).

Image analysis for indirect immunofluorescence.

Indirect immunofluorescence images were captured using Metamorph (Molecular Devices). Quantitative analysis of fixed-cell images was performed using ImageJ/FIJI (v1.53k). Regions of interest (ROI) were generated for MN and the PN in the same cell using customized ImageJ/FIJI macros as described in Liu et al, 2018[10]. Briefly, nuclear segmentation was performed using the best focal plane for the MN and PN based on Hoechst staining. The corresponding image masks were used to measure γH2AX, inosine, BAF, MPG, EdU and BrdU FI in the MN and PN. MN was defined as being “γH2AX positive” if the mean per pixel γH2AX IF of MN was more than 3 SD above the mean per pixel γH2AX FI of PN. The same approach was used to score α-inosine and TUNEL assay positivity. To identify MN NE rupture, we either used the accumulation of BAF or the loss of the nuclear import reporter RFP-NLS. The experiments where BAF accumulation was used to assess MN NE rupture were: Figs. 2b,3c–d, Extended Data Figs. 1b, 3b, 5, 7h, 9 e–h. In all other experiments we used RFP-NLS loss: Fig. 1h–i.

Western blots.

Cells were harvested by trypsinization, pelleted, washed in PBS and lysed in RIPA buffer (Boston Bioproducts, cat #: BP-115–500ML) on ice for 10 minutes and passed through a 27G 1/2 needle (0.4 mm x 40 mm) (BD cat #: 301629) several times to shear genomic DNA. The samples were mixed with a 1/3 volume of 4X Laemmli SDS-Sample Buffer (Boston Bioproducts, cat #: BP-110R) and denatured by heating at 100°C for 10 minutes.

Ice-chilled samples were centrifuged at maximum speed for 5 minutes at 4°C in a tabletop microfuge. The samples were separated on NUPAGE 4–12% Bis-Tris polyacrylamide gels (Life Technologies, cat #: NP0335BOX). The gels were transferred at 4°C by using a miniVE vertical electrophoresis system according to the manufacturer’s instruction. Odyssey Blocking Buffer (LI-COR) was used for membrane blocking and antibody dilution. Blots were incubated overnight at 4°C with primary antibodies (1:1000 unless otherwise specified with a 1:5000 α-GAPDH Ab to detect the loading control). Three washes were performed with TBST, followed by incubation with fluorescent secondary antibodies (LI-COR) for 1 hour at room temperature, followed by an additional 3 TBST washes. Membranes were visualized using a ChemiDoc MP Imaging System (Bio-Rad).

Purification of micronuclei.

The protocol used in this study was modified from Shimizu et al[24]. We used U2OS cells for purification because of higher MN DNA yield than for RPE-1 cells. 24 hours before harvesting the cells, 1.5 μM of MPS1 inhibitor was added to U2OS cells at 40 to 50% confluence. 2–4 X 10^9 cells were harvested by using trypsinization and washed twice with serum free DMEM media. The cells were pelleted by centrifugation at 1200 rpm for 5 minutes. Cell pellets were resuspended in 20 ml pre-warmed serum free DMEM medium containing cytochalasin B (10 μg/mL) and incubated for 30 minutes at 37°C. Cells were collected by centrifugation at 1200 rpm for 5 minutes. To prevent oxidation and adenine deamination during MN isolation, 0.35 mM 8-hydroxyquinoline (Sigma-Aldrich, cat #: 252565) and 5 μg/mL pentostatin (Tocris, cat #: 2033) were included in all the buffers used for the following steps[47,48]. Cells were resuspended in 10 mL pre-chilled lysis buffer (10 mM Tris-HCH, 2 mM Mg-acetate, 3 mM $CaCl_2$, 0.32 M sucrose, 0.1 mM EDTA, 1 mM DTT, 0.1% NP-40 substitute, 0.15 mM spermine, 0.75 mM spermidine and 10 μg/mL cytochalasin B, pH8.5). Four to five strokes with a Dounce homogenizer equipped with a loose-fitting pestle, were performed to break the cells and release the PN and MN. A few μL of homogenate were mixed with equal volume of DAPI solution (2 μg/mL in PBS) and examined under a fluorescence microscope to verify the efficiency of cell breakage. Homogenates were mixed with an equal volume (~11 mL) of pre-chilled 1.8 M sucrose buffer (10 mM Tris-HCH, 1.8 M sucrose, 5 mM Mg-acetate, 0.1 mM EDTA, 1 mM DTT, 0.3% BSA, 0.15 mM spermine, 0.75 mM spermidine and 10 μg/mL cytochalasin B, pH8.0). 10 ml of the mixed homogenate was then laid onto the top of a sucrose cushion (20 ml 1.8 M sucrose buffer as above at the bottom, 15 mL of 1.4 M sucrose buffer on top layer) in a 50 mL Falcon tube. Samples were centrifuged in a Sorvall legend RT+ centrifuge at 944 g for 20 minutes at 4°C. The top first 3 mL, containing cell debris and a few MN was discarded. The next 12 mL were taken to recover most MN. This step roughly separated MN from PN. At the interface between the sucrose layers was a PN fraction. Half of this fraction was carried through the steps below to obtain the final PN fraction. At this stage, the MN fraction was contaminated with a significant number of PN.

Further purification of MN was achieved by layering the crude MN fraction (~6 mL per tube) on 4.7 mL, 1.8 M sucrose cushion buffer followed by centrifugation at 14000 rpm for 90 minutes at 4°C using an SW40 rotor. The supernatant was discarded and the white interface between the two buffer layers was collected. This material was resuspended in buffer (10 mM Tris-HCH, 5 mM Mg-acetate, 0.1 mM EDTA, 1 mM DTT, 0.3% BSA, 0.15 mM spermine, 0.75 mM spermidine and 10 μg/mL cytochalasin B, pH8.0). 1 mL of the suspension was layered on top of an 11 mL linear sucrose gradient (1.0 to 1.8 M sucrose buffer) in a 15 mL tube. The samples were centrifuged in a Sorvall legend RT+ centrifuge at 530 g for 15 minutes at 4°C. 1 mL fractions from the top were collected and the purity of MN in each fraction was examined by fluorescence microscopy as described above. The first 3 ml contained MN, largely free of PN. These fractions were combined and diluted 5-fold with PBS. The samples were centrifuged in a Sorvall legend RT+ centrifuge at 944 g for 20 minutes at 4°C. The supernatant was discarded, and the pellet was resuspended with PBS and centrifuged in Sorvall Legend Micro 17R centrifuge at 2000 rpm for 10 minutes at 4°C. The pellets were collected and stored at −80°C.

Dot blot assays.

PN and MN DNA were isolated from the above-described fractions using a Qiagen Genomic DNA kit (Qiagen, cat #: 69504). A 1/10 volume of RNaseA (10 mg/mL, Life Technologies, cat #: EN0531) was added to the sample for incubation 10 minutes at 37 °C before adding proteinase K. For RNaseH treatment, 60 U of RNaseH (Takara Bio, cat #: 2150B) was used for 2 μg PN (800ng MN) DNA with RNaseH buffer (NEB, cat #: M0297L) for 4 hours at 37 °C. For inosine dot blots, in order to eliminate the signal from RNA, RNaseA treated PN and MN DNA samples were additionally digested with RNaseH and RNaseIII. In a 60 μL reaction, 2 μg PN or 800 ng MN DNA was incubated with 4 U of Shortcut RNaseIII (NEB, cat #: M0245L) and 60 U of RNaseH in RNaseH buffer for 4 hours at 37 °C. After digestion, DNA was extracted with chloroform/isoamyl alcohol and quantified with the Qubit™ dsDNA HS Assay kit (Life Technologies, cat #: Q32854). 200 ng of DNA was resuspended in 50 to 100 μL of nuclease-free water and loaded onto a nylon GeneScreen Plus membrane (PerkinElmer, cat #: NEF988001pk) using a Bio-Dot Microfiltration Apparatus (Bio-Rad, cat #: 1706545). The membrane was UV-crosslinked for 10 minutes and blocked with Intercept® blocking buffer (LI-COR, cat #: 927–60001) for 1 hour at room temperature. Primary antibody (S9.6 1:1000 or α-inosine 1:1000) was added to the blocking buffer and incubated overnight at 4°C with gentle shaking. The membrane was washed with TBST three times. Secondary antibodies (IRDye 800CW or IRDye 680RD) were added to the blocking buffer and incubated for 1 hour at room temperature with gentle shaking. The membrane was washed three times with TBST. The membrane was imaged with ChemiDoc™ MP Imaging System (Bio-Rad) and the images were quantified by using Image Lab3 (Bio-Rad). For all of the dot blot image analysis, the maximal signal was <50% of the saturation detection limit for the instrument and therefore within the linear range. To evaluate sample loading, the membrane was stripped and blotted with antibodies recognizing either dsDNA, RNA-DNA hybrids or dsRNA. The membrane was stripped with Restore Western blot Stripping buffer (Thermo Fisher, cat #: 21063) for 15 minutes with rigorous shaking. The membrane was washed three times with TBST before blocking with blocking buffer prior to an overnight 4°C incubation in secondary antibody.

MPG-APE oligonucleotide cleavage and dot blot assays.

We used the same substrates and protocol, with minor modifications, described in Liu et al[36]. Substrates with one strand containing a 5’ fluorescent label (fluorescein amitide or

FAM, 38 bp dsDNA, DNA-RNA and dsRNA with or without hypoxanthine on one of the strands, 400 nM) were incubated with 5 U of MPG (NEB, cat #: M0313) at 37°C for time intervals spanning 5 to 120 minutes in a buffer containing 50 mM HEPES, pH 8.0, 100 mM KCL, 1 mg/mL BSA, and 1 mM DTT. After the MPG digestion, 50 U of APE1(NEB, cat #: M0282L) and 5 mM MgCl2 were added to the reaction for another incubation of 5 minutes followed by 0.5 volume of chloroform exaction (chloroform: iso-amyl alcohol, 24:1). The oligonucleotide cleavage assay relies on APE1 cleavage of abasic sites, which is well established for abasic sites in DNA. Liu et al[36] concluded that APE1 can cleave abasic sites in RNA, but this activity was reduced relative to the APE1 activity towards abasic sites in DNA. To circumvent this complication and assay MPG-mediated removal of dI or I independently from APE1, MPG was incubated with the same oligonucleotide substrates as for the APE1 cleavage assay, for the same time intervals. We then used the dot blot assay to identify MPG-mediated removal of the hypoxanthine base from either dI or I. Note that the control samples in Extended Data Fig. 10c were not FAM labeled, instead, the nucleic acids were detected by SYBR™ GOLD. Extracted nucleotides were quantified using Qubit ssDNA quantification kit (Life Technologies, cat #: Q10212). The same amount of nucleic acid (20 ng for FAM labeled substrates) from each time-point were mixed with an equal volume of formamide dye (98% formamide, 10 mM EDTA, 0.1% bromophenol blue and 0.1% xylene cyanol) and denatured for 5 minutes at 95°C. Nucleotides were then separated on a 15% TBE-Urea gel (NovexTM TBE-Urea gel, cat #: EC6885BOX) with constant voltage of 300 V and imaged on ChemiDocTM MP Imaging System (Bio-Rad). Cleavage efficiency was calculated as cleavage product fluorescence intensity divided by the total fluorescence intensity of the lane, including the uncut band (38 nt) and the cleavage band (15 nt). For samples without FAM-labeling, the gels were stained with SYBR™ Gold nucleic acid dye (Invitrogen, S11494) for 15 minutes at room temperature. Imaging and analysis were performed as described above for the FAM-labeled samples.

Statistical analysis and Reproducibility.

Statistical analyses were performed using Prism (GraphPad software Inc.). Non-parametric tests (Two-tailed Mann–Whitney U test) were performed on all comparisons of two scatter plot data sets. For bar graphs comparing two samples (aggregated from three or more replicate experiments), unpaired t-tests were performed. For multiple comparisons one-way ANOVA were performed (Tukey or Dunnett tests, depending on the specific comparisons being made). For all scatter plots, the bars show the mean value with a 95% CI. For all bar graphs, what is shown is the mean and standard deviation. No statistical methods were used to predetermine sample size. The experiments were not randomized, and the investigators were not blinded to allocation during experiments and outcome assessment. All the Western blots and dot blots have been repeated at least three times (Fig. 1b, f, 2c and 3b, e and f, 4b and c, Extended Data Fig. 1c, 2a, 3a, 4a and c, 6a, g and k, 8d, e and h, 9a and b, 10c and d), and representative immunofluorescence images have been chosen from over 100 samples in each experiments; the experiments were repeated at least three times with independent biological replicates (Fig. 1d and h, Fig. 2b and d, 3a and c, Extended Data Fig. 1g, 3b, 5, 7a, 8b and 9d).

Extended Data

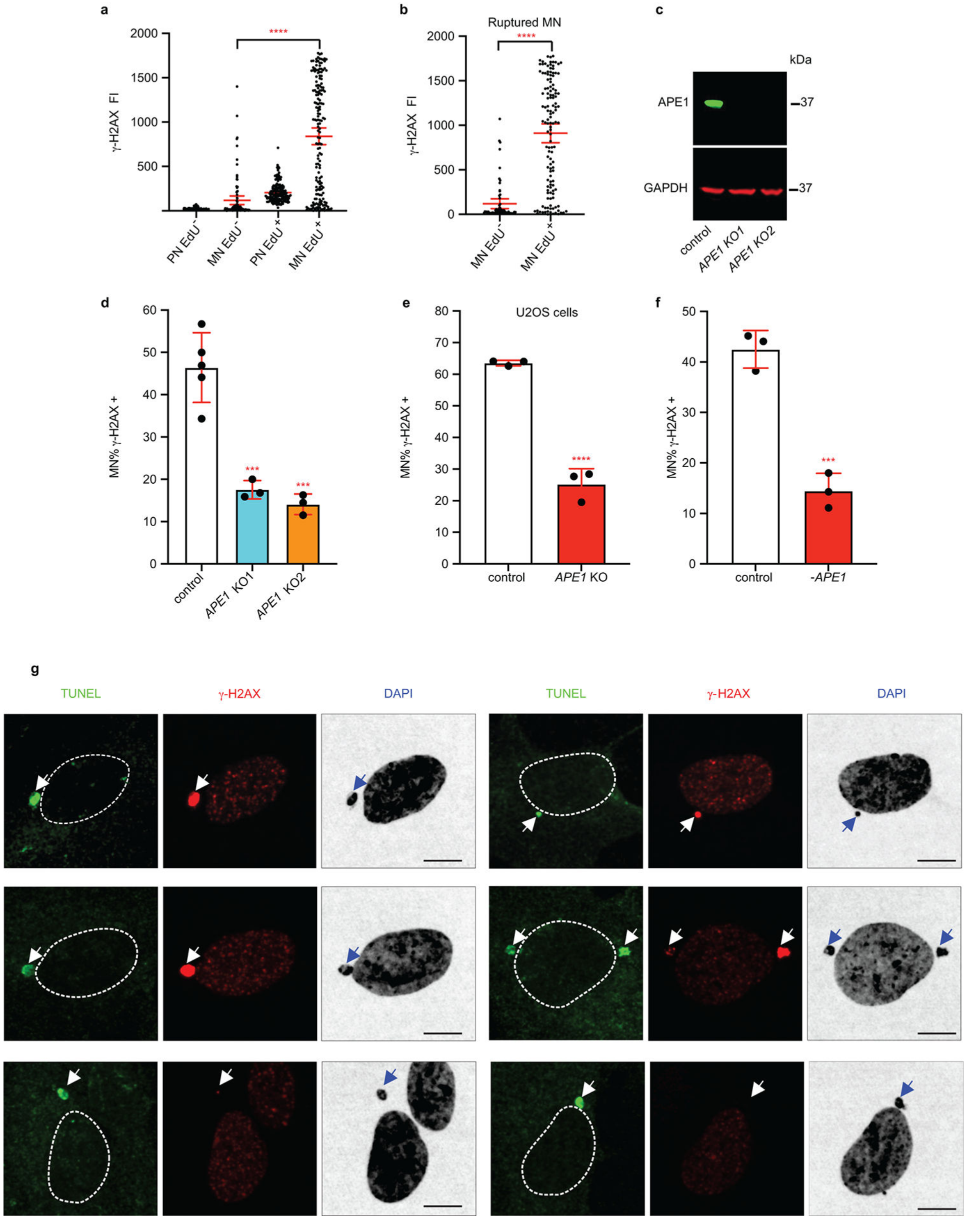

Extended Data Figure 1. DNA damage in micronuclei depends on APE1 endonuclease.

(**a**) γ-H2AX fluorescence intensity (FI, arbitrary units) in all PN and MN (ruptured and unruptured) before (EdU$^-$) and after S phase entry (EdU$^+$). RPE-1 cells were synchronized as in Fig. 1a (mean with 95% CI, ****$P<0.0001$, Ordinary one-way ANOVA with Tukey's multiple comparisons test, EdU$^-$: n=95; EdU$^+$: n=171).

(**b**) γ-H2AX FI in ruptured MN, comparing EdU$^+$ and EdU$^-$ cells, as in Extended data Fig. 1a (mean with 95% CI, ****$P<0.0001$, Two-tailed Mann-Whitney U test, EdU$^-$: n=65; EdU$^+$: n=131).

(**c**) Western blot to detect APE1 in control and two knockout clones. GAPDH is the loading control.

(**d**) Aggregated data from three replicates showing the % of γ-H2AX positive MN (> 3 SD above PN background) in control and two *APE1* knockout clones (mean with SD, ***P=0.0004 (control vs. *APE1* KO1), ***P=0.0002 (control vs. *APE1* KO2), Ordinary one-way ANOVA with Dunnett's multiple comparisons test control: n=687; *APE1* KO1: n=472; *APE1* KO2: n=519).

(**e**) Aggregated data from three replicates of control and *APE1* knockout U2OS cells, synchronized as in Fig. 1a, after p53 RNAi (mean with SD, ***P=0.0002, two-tailed unpaired t-test. control: n=346; *APE1* KO: n=318).

(**f**) Aggregated data from three replicates for the example in Fig. 1c. (mean with SD, ***P=0.0007, two-tailed unpaired t-test, control: n=423; -APE1: n=457).

(**g**) Representative images of RPE-1 cells co-stained to detect TUNEL signal (green) and γ-H2AX (red). Of TUNEL positive MN (n=391), 70.3% are also γ-H2AX positive. Dotted white lines outline the PN. Arrow heads: MN.

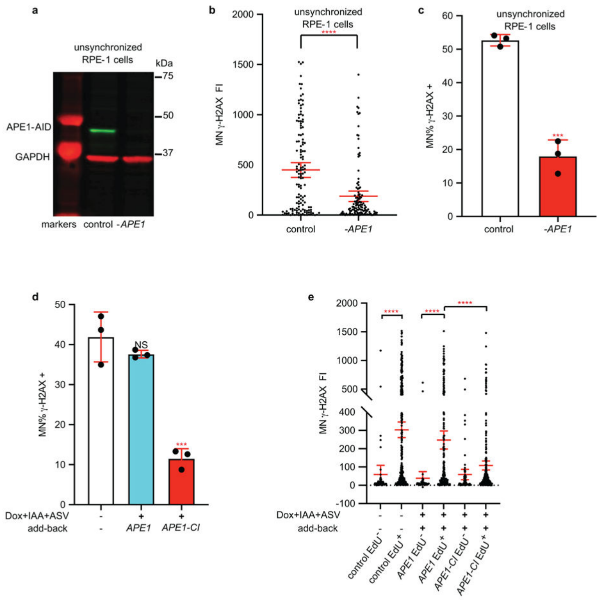

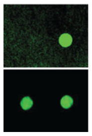

Extended Data Figure 2. DNA damage in micronuclei in synchronized and unsynchronized cells depends on the catalytic activity of APE1.

(**a**) APE1-AID-SMASh degradation in unsynchronized RPE-1 cells. Control: no drugs; -APE1: 12 hours drug treatment prior to western (Dox, IAA and ASV). GAPDH is the loading control.

(**b**) MN γ-H2AX FI with or without APE1 degradation in unsynchronized RPE-1 cells (mean with 95% CI, ****$P<0.0001$, Two-tailed Mann-Whitney U test, control: n=133; -APE: n=123).

(**c**) Aggregated data from three replicates for MN DNA damage after APE1-AID-SMASh degradation in unsynchronized RPE-1 cells. Drugs to induce APE1-AID-SMASh degradation were added 12 hours prior to treatment with MPS1i to generate MN. After 48 hours cells were fixed and DNA damage was assessed (mean with SD, ***P=0.0003, two-tailed unpaired t-test, control: n=379; -APE1: n=353).

(**d**) Aggregated data from three replicates for the example in Fig. 1g (mean with SD, NS: P=0.3606, ***P=0.0002, Ordinary one-way ANOVA with Dunnett's multiple comparisons test, control: n=424; *APE1* add-back: n=392; *APE1-CI* add-back: n=400).

(**e**) MN γ-H2AX FI as shown in Fig. 1g but comparing labeling in EdU+ and EdU- cells for the indicated samples (mean with 95% CI, ****P<0.0001, Ordinary one-way ANOVA with Tukey's multiple comparisons test. N values from left to right: n=53, 288, 41, 177, 71 and 280).

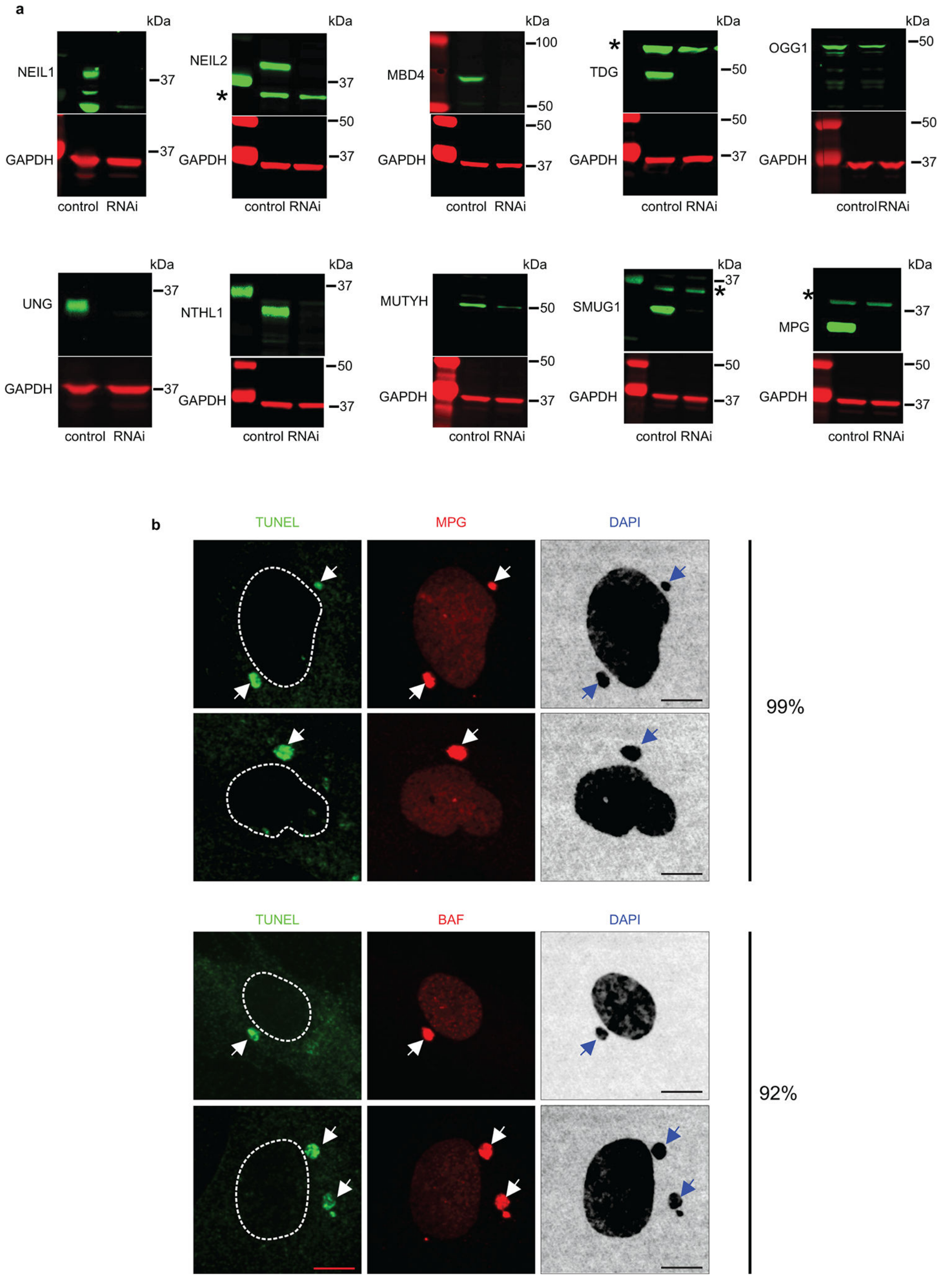

Extended Data Figure 3. Western blot verification of glycosylase knockdown efficiency and MPG accumulation co-localizes with ruptured, TUNEL-positive MN.

(**a**) Western blots to detect the indicated glycosylases. Shown are the control and 72 hours RNAi treatments of RPE-1 cells. Asterisk indicates background bands. GAPDH is the loading control. Uncropped images are shown in the Source Data file.

(**b**) MPG accumulation co-localizes with ruptured, TUNEL-positive MN in RPE-1 cells. Top two panels: TUNEL-labeling is green; MPG-labeling is red. Of visibly TUNEL positive MN (n=325), 99% display heavy accumulation of endogenous MPG. Bottom two panels:

TUNEL-labeling is green; BAF-labeling is red. Of visibly TUNEL positive MN (n=334), 92% display heavy accumulation of BAF, a marker for NE rupture. Arrow heads: MN.

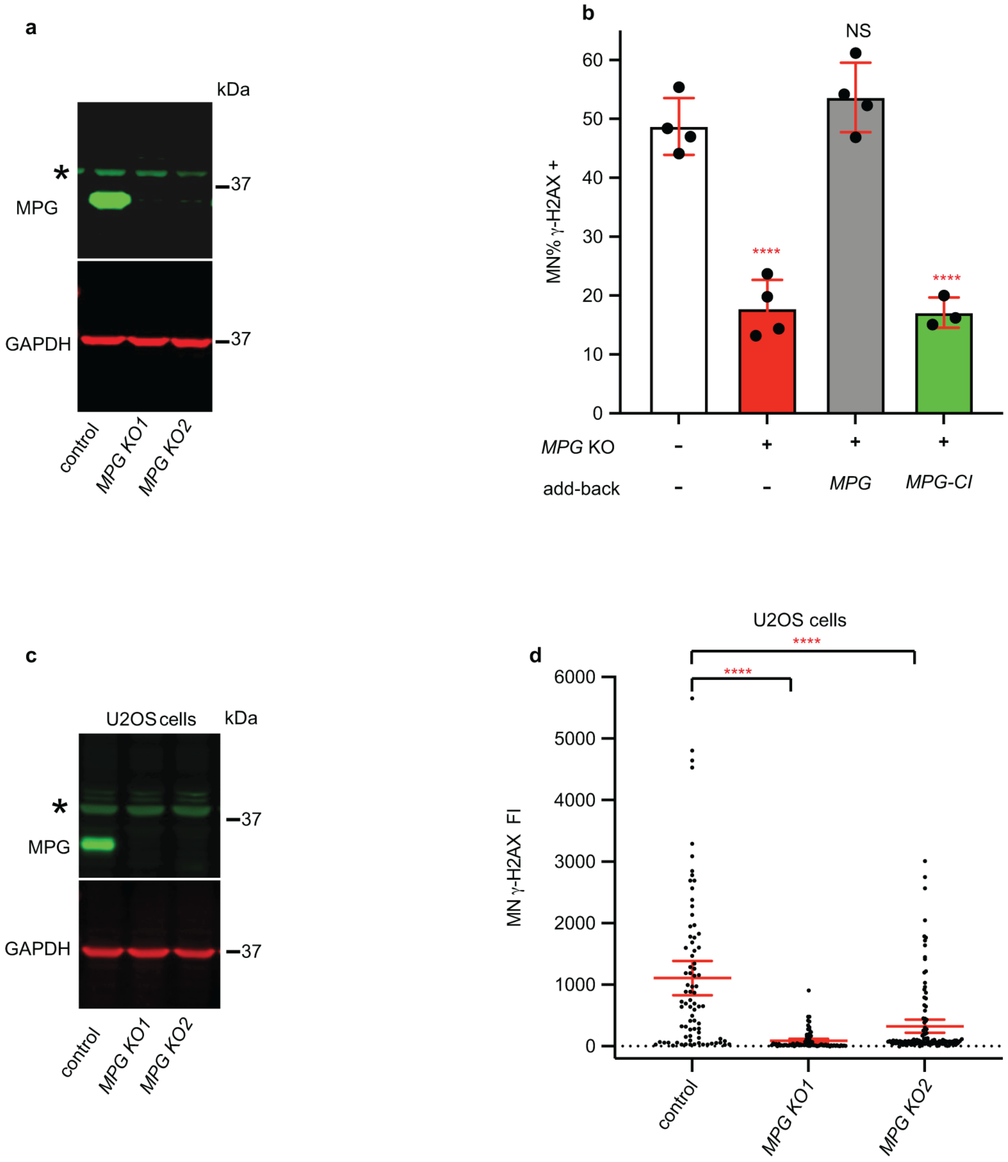

Extended Data Figure 4. MPG catalytic activity is required for DNA damage in micronuclei in RPE-1 and U2OS cells.

(**a**) Western blots to detect MPG in control and two knockout clones. Asterisk indicates background bands. GAPDH is the loading control.

(**b**) MPG catalytic activity is required to generate MN DNA damage. Aggregated data from three replicates for MN DNA damage in the indicated cell lines with the indicated add-back constructs as in Fig. 2g (mean with SD; NS, $P=0.8326$; ****$P<0.0001$; Ordinary one-way ANOVA with Dunnett’s multiple comparisons test. N values from left to the right: n=264, 472, 392, and 287).

(**c**) Western blots to detect MPG in control and two knockout U2OS clones. GAPDH is loading control. Asterisk indicates background bands. GAPDH is the loading control.

(**d**) MN γ-H2AX FI in control and *MPG* knockout U2OS cells. MN γ-H2AX FI measurements for control and two *MPG* KO clones synchronized as in Fig. 1a, after p53 RNAi (mean with 95% CI, *****P*<0.0001, Ordinary one-way ANOVA with Dunnett's multiple comparisons test. control: n=80; *MPG KO1*: n=76; *MGP KO* 2: n=119).

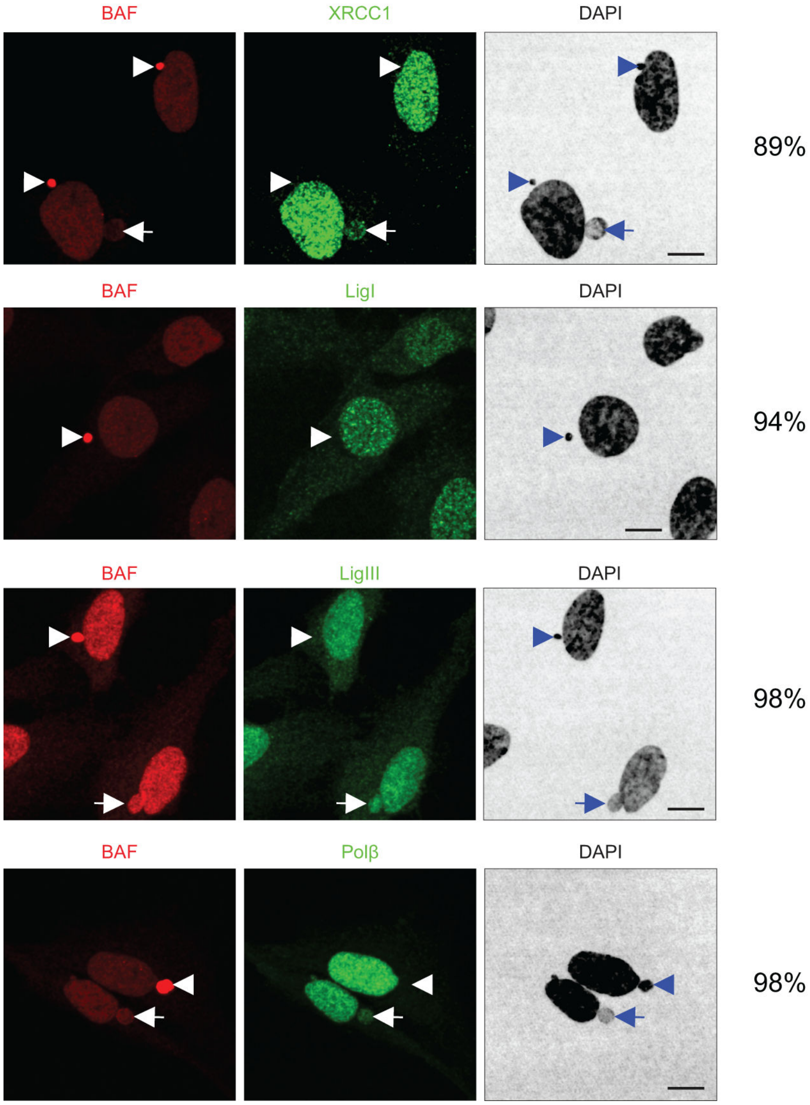

Extended Data Figure 5. BER factors downstream of ssDNA nick generation are lost from ruptured micronuclei.

Representative images of RPE-1 cells stained for BAF and the indicated BER components. White arrowheads: ruptured MN that accumulate BAF lose BER components. White arrows: intact MN retain detectable BER components. Number on the right on each panel is showing the percentage of ruptured MN that visibly lose respective BER factors: 89.4% for XRCC1(n=132), 94.2% for LigI (n=241), 98.2% for LigIII (n=230) and 98% for Polβ (n=155).

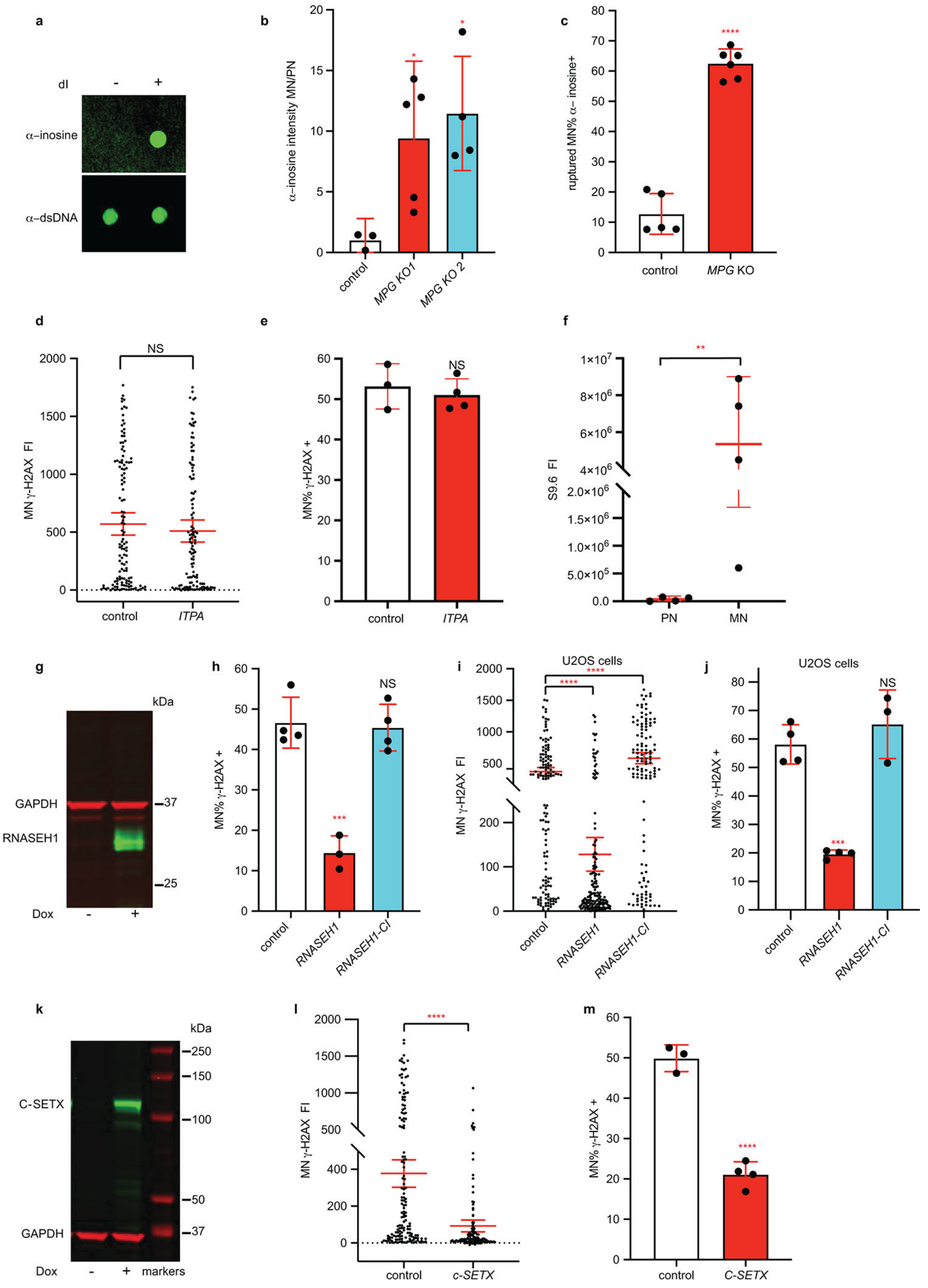

Extended Data Figure 6. RNA-DNA hybrids contribute to DNA damage in micronuclei.

(**a**) Dot blot showing that the α-inosine antibody recognizes dI in dsDNA oligonucleotides. α-dsDNA is the loading control.

(**b**) dI accumulates on MN in *MPG* KO cells. Aggregated data from four biological replicates to detect α-inosine signal from purified PN and MN from wild-type and two *MPG* KO clones of U2OS cells. (mean with SD, Ordinary one-way ANOVA with Dunnett's multiple comparisons test, **P*=0.0465 (*KO*1), **P*=0.0212(*KO*2)).

(**c**) Aggregated data from three replicate experiments for the example in Fig. 3c and 3d. Inosine$^+$ ruptured MN were defined as having >3SD of the PN mean value (mean with SD, *****P*<0.0001, two-tailed unpaired t-test. control: n=577; *MPG* KO: n=882).

(**d**) Overexpression of ITPA does not reduce DNA damage in MN. MN γ-H2AX FI measured from control or cells overexpressing ITPA. ITPA expression was induced with CMV promoter (mean with 95% CI, NS, *P*=0.3736, Two-tailed Mann-Whitney U test, control: n=129; *ITPA*: n=124).

(**e**) Aggregated data from three replicate experiments to detect MN DNA damage after ITPA overexpression as in Extended Data Fig. 6d (mean with SD, NS, *P*=0.2306, two-tailed unpaired t-test. control: n=274; *ITPA*: n=372).

(**f**) Data from four independent replicates of the experiment in Fig. 3e, showing S9.6 enrichment in MN over PN. Y axis shows S9.6 labeling intensity for PN and MN fractions from four biological replicates (mean with SD, ***P*=0.0020, unpaired t test after log transformation).

(**g**) Western blot to detect induced expression of RNaseH1 (Tet-on system). GAPDH is the loading control.

(**h**) RNaseH1 over expression suppresses MN DNA damage. Aggregated data from three replicate experiments for the example shown in Fig. 3g (mean with SD, NS, *P*=0.9355, ****P*=0.0001, Ordinary one-way ANOVA with Dunnett's multiple comparisons test. control: n=399; *RNaseH1*: n=391; *RNaseH1-CI* (D210N): n=548).

(**i**) Overexpression of RNaseH1 suppresses MN DNA damage in U2OS cells. MN γ-H2AX FI from cells with or without overexpression of RNaseH1 or a catalytically inactive mutant (D210N) in U2OS cells (mean with 95% CI, *****P*<0.0001, Ordinary one-way ANOVA with Dunnett's multiple comparisons test. control: 141; *RNASEH1*: n=168; *RNASEH1-CI*: n=125).

(**j**) Overexpression of RNaseH1 suppresses MN DNA damage in U2OS cells. Summary of three biological replicates as in Extended data Fig. 3i above (mean with SD, NS, *P*=0.3963, *** *P*=0.0002, Ordinary one-way ANOVA with Dunnett's multiple comparisons test. control: n=548; *RNASEH1*: n=470; *RNASEH1-CI*: n=380).

(**k**) Western blot to detect induced expression of the C-terminal catalytic domain of SETX (C-SETX, Tet-on system). GAPDH is the loading control.

(**l**) C-SETX overexpression suppresses MN DNA damage. MN γ-H2AX FI in cells with or without overexpression of C-SETX (mean with 95% CI, *****P*<0.0001, Two-tailed Mann-Whitney U test. control: n=149; *C-SETX*: n=118).

(**m**) Aggregated data from three replicates for overexpression of C-SETX as in Extended data Fig. 3l (mean with SD, *****P*<0.0001, two-tailed unpaired t-test. control: n=392; *C-SETX*: n=579).

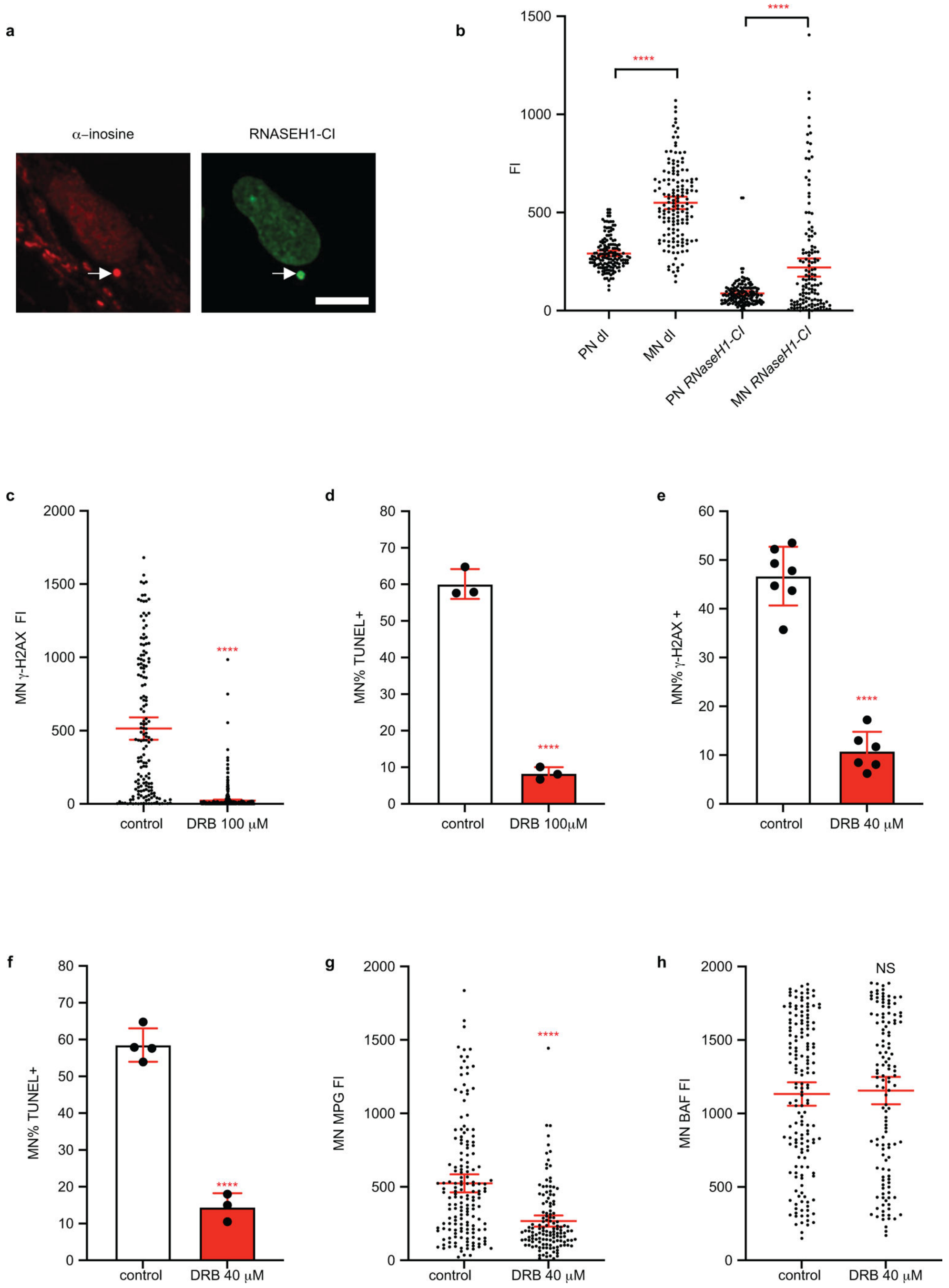

Extended Data Figure 7. Inhibition of transcription (DRB) reduces micronuclei DNA damage.

(**a**) Representative images showing that α-inosine signal colocalizes with the accumulation of *RNaseH1-CI* (marking RNA-DNA hybrids) on MN in *MPG* KO RPE-1 cells.

(**b**) Fluorescence intensity of α-inosine and RNaseH1 CI signal of cells shown in (a) above (mean with 95% CI, *****P*<0.0001, Ordinary one-way ANOVA with Tukey's multiple comparisons test. n=81cells were analyzed). This shows that MN that accumulate RNA-DNA hybrids also have high-level α-inosine labeling.

(**c**) MN γ-H2AX FI measured from control or cells treated with 100 μM DRB, which prevents S phase entry, almost completely blocks MN DNA damage (mean with 95% CI, ****P<0.0001, Two-tailed Mann-Whitney U test, control: n=151; DRB: n=266).

(**d**) % of TUNEL positive MN in control and cells treated with 100 μM DRB. Aggregated data from 3 replicates from a similar experiment to (c) above but with TUNEL-labeling (mean with SD, ****P<0.0001, two-tailed unpaired t-test, control: n=490; DRB 100 μM: n=928).

(**e**) % γ-H2AX positive MN in control and cells treated with 40 μM DRB. Aggregated data from 6 replicates from the experiment in Fig. 3h (mean with SD, two-tailed unpaired t-test, ****P<0.0001, control: n=910; DRB 40 μM: n=990). Note 40 μM DRB allows some cells to progress into S phase; only S phase cells were analyzed (visibly EdU positive PN).

(**f**) % of TUNEL positive MN in control and cells treated with 40 μM DRB. Aggregated data from 3 replicates from a similar experiment to Fig. 3h but with TUNEL-labeling instead of γ-H2AX (mean with SD, two-tailed unpaired t-test, ****P<0.0001, control: n=642; DRB 40 μM: n=525).

(**g**) Transcription is required for maximal accumulation of MPG on ruptured MN. Similar to the experiment shown in Fig. 3h (mean with 95% CI, ****P<0.0001, Two-tailed Mann-Whitney U test, control: n=161, DRB 40 μM: n=133).

(**h**) DRB treatment does not affect MN rupture frequency. Similar to experiments shown in Fig. 3h (mean with 95% CI, NS, P=0.5889, Two-tailed Mann-Whitney U test, control: n=161, DRB 40 μM: n=133).

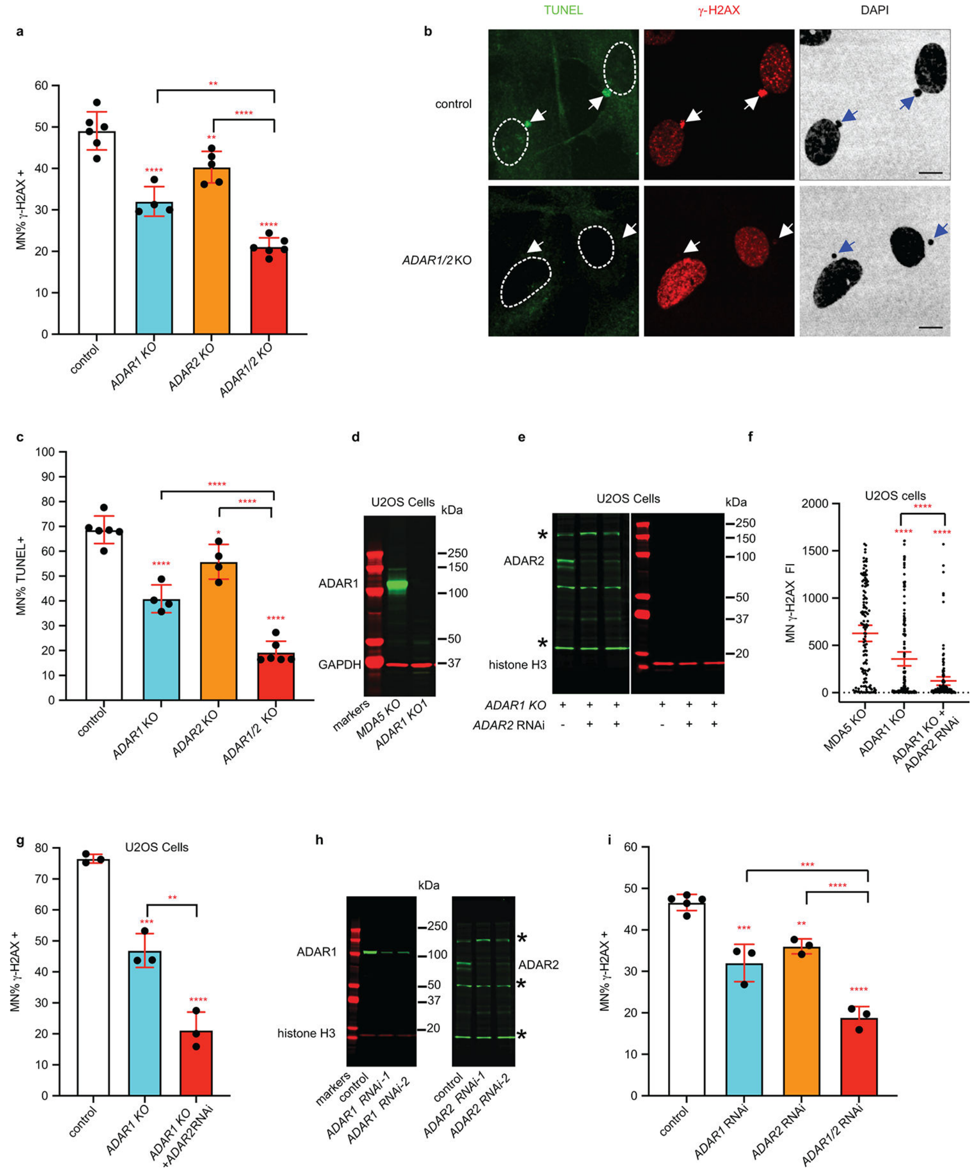

Extended Data Figure 8. ADARs mediate micronuclei DNA damage.

(**a**) ADAR1 and ADAR2 are required for MN DNA damage in *MDA5* KO *TP53* KO (control) RPE-1 cells. Aggregated data from three or more replicates of the experiment to detect MN DNA damage in the indicated cell lines (mean with SD, $**P=0.0048$ (*ADAR2* KO vs control), $**P=0.0012$ (*ADAR1* KO vs *ADAR1/2* KO), $****P<0.0001$, Ordinary One-way ANOVA with Tukey's multiple comparisons test. control: n=549; *ADAR1* KO: n=387; *ADAR2*: n=318; *ADAR1/2* KO: n=1266).

(**b**) Representative images of RPE-1cells of *MDA5* KO (control) and *MDA5*, *ADAR1*, *ADAR2* triple KO (*ADAR1/2* KO). TUNEL assay: green; γ-H2AX: red; white arrows: MN. Dotted white lines outline the PN.

(**c**) ADAR1 and ADAR2 are required for MN DNA damage as assayed by TUNEL-labeling. Aggregated data from three or more replicates to detect MN DNA damage as in (a) above. (mean with SD, $*P=0.0122$, $****P<0.0001$, Ordinary One-way ANOVA with Tukey's multiple comparisons test. control: n=881; *ADAR1* KO: n=531; *ADAR2*: n=525; *ADAR1/2* KO: n=978).

(**d**) Western blot showing ADAR1 steady-state levels in control and an *ADAR1* knockout U2OS cell line. GAPDH is the loading control.

(**e**) Western blot to detect ADAR2 from nuclear extracts after ADAR2 RNAi in *MDA5* KO *ADAR1* KO U2OS lines. Asterisk: background bands; histone H3 is the loading control.

(**f**) MN DNA damage in *ADAR1* KO as compared to *ADAR1* KO plus *ADAR2* RNAi in *MDA5* KO U2OS cells (mean with 95% CI, ****$P<0.0001$, Ordinary one-way ANOVA with Tukey's multiple comparisons test. control: n=131; *ADAR1* KO: n=160; *ADAR1* KO + *ADAR2* RNAi: n=132).

(**g**) Aggregated data from three replicates of the experiment in (f) above, to detect MN DNA damage in the indicated cell lines (mean with SD, **$P=0.0013$, ***$P=0.0006$, ****$P<0.0001$, Ordinary one-way ANOVA with Tukey's multiple comparisons test. control: n=437; *ADAR1* KO: n=452; *ADAR1* KO + *ADAR2* RNAi: n=417).

(h) Western blot showing the steady-state levels of ADAR1 or ADAR2 from nuclear extracts after double knockdown of *ADAR1* and *ADAR2* in *TP53* knockout RPE-1 cells. Left, ADAR1 levels after RNAi; Right, ADAR2 levels after RNAi. Asterisk: background bands; histone H3 is the loading control.

(i) ADARs mediate micronuclei DNA damage shown by RNAi in MDA5-proficient RPE-1 cells. Aggregated data from three replicates to detect MN DNA damage in the indicated RNAi-treated *TP53* KO RPE-1 cells (control), as in (h) above (mean with SD, **$P=0.0017$, ***$P=0.0001$(control vs. ADAR1 RNAi), ***$P=0.0008$ (ADAR1 RNAi vs. ADAR1 plus ADAR2 RNAi), **** $P<0.0001$, Ordinary one-way ANOVA with Tukey's multiple comparisons test. control: n=882; *ADAR1* RNAi: n=456; *ADAR2 RNAi*: n=573; *ADAR1/2* RNAi: n=544). Note: this experiment is a control for Fig. 3i and Extended Data Fig. 8a, c. The cell line used in Fig. 3i and Extended Data Fig. 8a, c lacks MDA5 to enable survival of ADAR-deficient RPE-1 cells. The cell line used here lacks p53 but is proficient for MDA5. Therefore, MDA5 loss does not affect MN DNA damage.

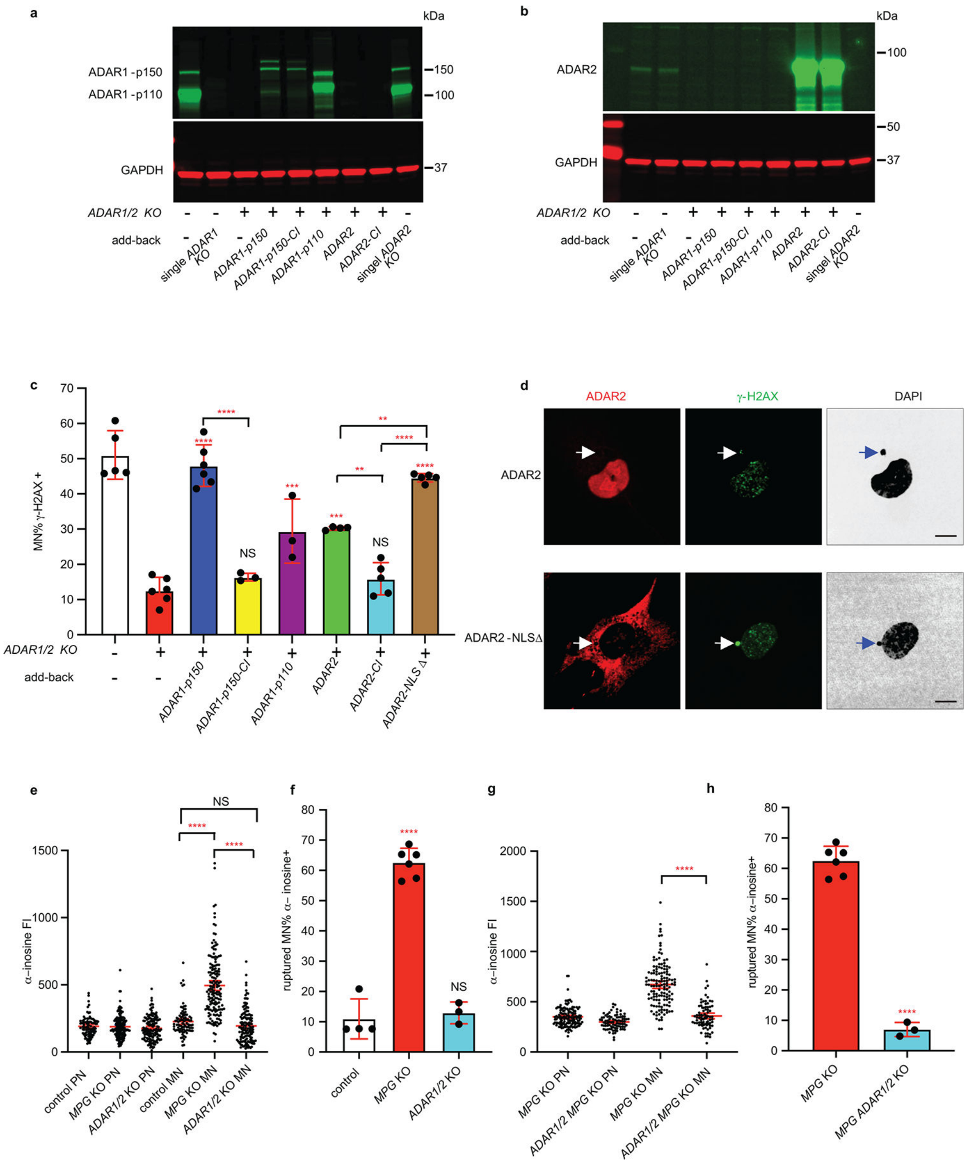

Extended Data Figure 9. Cytoplasmic localization and the catalytic activity of ADAR1 and ADAR2 are required for micronuclear DNA damage.

(**a**) Western blot to detect expression from the indicated ADAR1 add-back constructs in the indicated cell lines. GAPDH is the loading control.

(**b**) Western blot to detect ADAR2 as in (a). GAPDH is the loading control.

(**c**) Cytoplasmic localization of ADAR1 and ADAR2 deaminase activity is required to optimally promote MN DNA damage. Aggregated data from three or more replicates to detect MN DNA damage in the indicated cell lines with the indicated add-back constructs as in Fig. 3i (mean with SD, all the add-backs were compared with the *ADAR1/2* KO unless specified on the graph. Ordinary one-way ANOVA with Tukey's multiple comparisons test, NS, P=0.9528 (*ADAR1-p150-CI* vs. *ADAR1/2 KO*), NS, P=0.9488 (*ADAR2-CI* vs. *ADAR1/2 KO*), **P=0.0032 (*ADAR2* vs. *ADAR2-CI*), **P=0.0032 (*ADAR2* vs. *ADAR2-NLSΔ*), ***P=0.0009 (*ADAR1-p110* vs. *ADAR1/2 KO*),***P=0.0001(*ADAR2* vs. *ADAR1/2 KO*), ****P<0.0001. N values from left to right: n=718, 1041, 641, 417, 182, 497, 653 and 502). ADAR1-p150 and ADAR1-p100 are different isoforms of ADAR1 p150 is primarily cytoplasmic whereas p110 is primarily nuclear. The add-back variants have the following mutations: *ADAR1-p150-CI* (H908N, E912A), *ADAR2-CI* (E396A), and *ADAR2-NLS*Δ (deletion of amino acids 48–72).

(**d**) Representative immunofluorescent images showing the cellular localization of ADAR2 add-back constructs in the *ADAR1/2* KO cell line. The proteins expressed from the add-back constructs are indicated on the left. White arrows: MN.

(**e**) α-inosine signal accumulation on ruptured MN requires ADAR1 and ADAR2. Inosine FI was measured in the indicated cell lines (mean with 95% CI, NS, P=0.4863, ****P<0.0001, Ordinary one-way ANOVA with Tukey's multiple comparisons test. control: n= 91; *MPG* KO: n= 155; *ADAR1/2* KO: n=135). Note: The cells were treated with RNaseT1, RNaseH1 and RNaseIII and denatured before the immunofluorescence staining. See Methods Indirect immunofluorescence microscopy section for details.

(**f**) Aggregated data from three replicates for the example shown in Extended Data Fig. 9e (mean with SD, NS, P=0.8362, ****P<0.0001, Ordinary one-way ANOVA with Dunnett's multiple comparisons test. control: n=448; *MPG KO*: n=882; *ADAR1/2 KO*: n=373).

(**g**) High level α-inosine signal in MN from *MPG* KO cells requires *ADAR1 and ADAR2*. α-inosine FI was measured in the indicated cell lines (mean with 95% CI, ****P<0.0001, Ordinary one-way ANOVA with Tukey's multiple comparisons test. *MPG* KO: n=134, *ADAR2* KO: n=85). Cells were treated as (e) above.

(**h**) Aggregated data from three replicates for the example in Extended Data Fig. 9g, above (mean with SD, **** P<0.0001, two-tailed unpaired t-test. *MPG* KO: n=882; *ADAR1/2 MPG KO*: n=341).

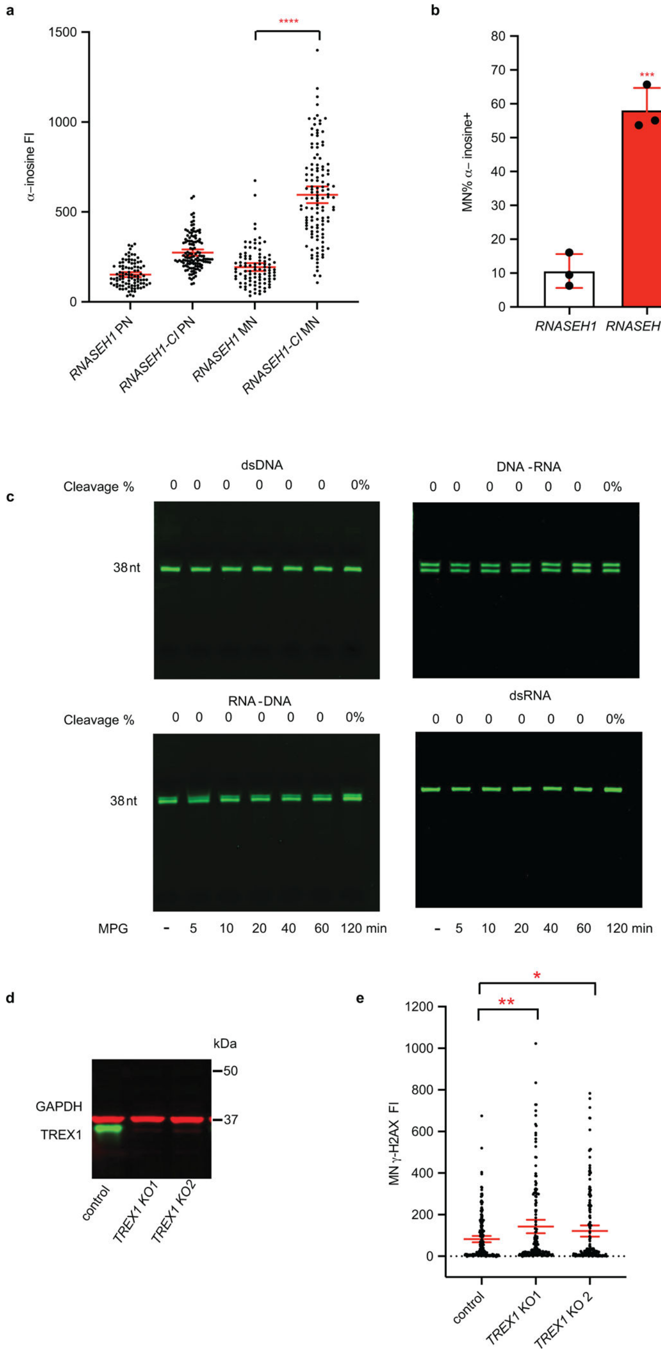

Extended Data Figure 10. RNA-DNA hybrids and α-inosine signal on micronuclei from MPG deficient cells; control for Fig. 4b; and TREX1 KO effect on MN DNA damage in RPE-1 cells.

(**a**) Overexpression of wild-type *RNASEH1,* but not *RNASEH1-CI*, suppresses MN α-inosine signal in *MPG* KO RPE-1 cells (mean with 95% CI, *****P*<0.0001, Ordinary one-way ANOVA with Tukey's multiple comparisons test. *RNASEH1*: n=91; *RNASEH1-CI*: n=121).

(**b**) Aggregated data from three replicates of the experiment in (a) above (mean with SD, two-tailed unpaired t-test, ****P*=0.0006, *RNASEH1*: n=404; *RNASEH1-CI*: n=348).

(c) MPG does not cleave bases from dsDNA, RNA:DNA hybrid, or dsRNA lacking dI or I. Images of Urea-PAGE gels from experiments where MPG and APE1 were incubated with the indicated substrates lacking dI or I, performed as in Fig. 4b. Nucleic acids are visualized with SYBR™ Gold. Shown is one example of three similar replicate experiments. This is a control experiment showing that there is no cleavage for any RNA or DNA-containing substrate if there is no nucleotide with a hypoxanthine base.

(**d**) Western blot showing TREX1 steady state levels in control and knockout clones. GAPDH is the loading control.

(**e**) The absence of TREX1 does not reduce MN DNA damage. MN γ-H2AX FI measurements for control and two *TREX1* KO clones synchronized as in Fig. 1a (mean with 95% CI, **P*=0.0466, ***P*<0.0015, Ordinary one-way ANOVA with Dunnett's multiple comparisons test. control: n=190; *TREX1 KO1*: n=155; *TREX1 KO* 2: n=166). The *TREX1* KO clones display a subtle increase in DNA damage relative to controls.

Supplementary Material

Refer to Web version on PubMed Central for supplementary material.

Acknowledgements

We thank D. Chowdhury, S. Hirsch, W. Johnson, I.-J. Lee, M. Liebowitz, N. Serbyn, J. Walter, G. Zhao, for comments on the manuscript, P. Beal, B. Daignan, W. Harper, P. Ly, L. Potano Vaites, J. Walter, Y. Wang, C.Z. Zhang and laboratory members for discussions, R. Davidowitz for artwork, W. Harper, D. Durocher and H. Hochegger for reagents. D.P. is an HHMI Investigator and is supported by NIH R01 CA213404-24 and a Research Investigator Award from the Lustgarten Foundation.

Data availability

The authors declare that the data supporting the findings of this study are available within the paper and its Supplemental Information files. Source data for all of the graphs (Fig. 1c, e. g, i; Extended Data Fig. 1a, b, d, e, f; Fig. 2a and e -g; Extended Data Fig. 2b–e; Fig. 3d and g–i; Extended Data Fig. 3b; Extended Data Fig. 4b, d; Extended Data Fig. 5; Extended Data Fig. 6b–f, h–j, l, m; Extended Data Fig. 7b–h; Extended Data Fig. 8a, c, f, g, i; Extended Data Fig. 9c, e–h; extended Data Fig. 10a,b and e) are provided with the online version of the paper. Raw imaging data from this study are available from the corresponding author upon request.

References

1. Maciejowski J & Hatch EM Nuclear Membrane Rupture and Its Consequences. Annu Rev Cell Dev Biol 36, 85–114, doi:10.1146/annurev-cellbio-020520-120627 (2020). [PubMed: 32692592]
2. Ly P & Cleveland DW Rebuilding Chromosomes After Catastrophe: Emerging Mechanisms of Chromothripsis. Trends Cell Biol 27, 917–930, doi:10.1016/j.tcb.2017.08.005 (2017). [PubMed: 28899600]
3. Stephens PJ et al. Massive genomic rearrangement acquired in a single catastrophic event during cancer development. Cell 144, 27–40, doi:10.1016/j.cell.2010.11.055 (2011). [PubMed: 21215367]
4. Korbel JO & Campbell PJ Criteria for inference of chromothripsis in cancer genomes. Cell 152, 1226–1236, doi:10.1016/j.cell.2013.02.023 (2013). [PubMed: 23498933]
5. Zhang CZ et al. Chromothripsis from DNA damage in micronuclei. Nature 522, 179–184, doi:10.1038/nature14493 (2015). [PubMed: 26017310]

6. Maciejowski J, Li Y, Bosco N, Campbell PJ & de Lange T Chromothripsis and Kataegis Induced by Telomere Crisis. Cell 163, 1641–1654, doi:10.1016/j.cell.2015.11.054 (2015). [PubMed: 26687355]
7. Ly P et al. Chromosome segregation errors generate a diverse spectrum of simple and complex genomic rearrangements. Nat Genet 51, 705–715, doi:10.1038/s41588-019-0360-8 (2019). [PubMed: 30833795]
8. Umbreit NT et al. Mechanisms generating cancer genome complexity from a single cell division error. Science 368, doi:10.1126/science.aba0712 (2020).
9. Hatch EM, Fischer AH, Deerinck TJ & Hetzer MW Catastrophic nuclear envelope collapse in cancer cell micronuclei. Cell 154, 47–60, doi:10.1016/j.cell.2013.06.007 (2013). [PubMed: 23827674]
10. Liu S et al. Nuclear envelope assembly defects link mitotic errors to chromothripsis. Nature 561, 551–555, doi:10.1038/s41586-018-0534-z (2018). [PubMed: 30232450]
11. Lee CY et al. Recognition and processing of a new repertoire of DNA substrates by human 3-methyladenine DNA glycosylase (AAG). Biochemistry 48, 1850–1861, doi:10.1021/bi8018898 (2009). [PubMed: 19219989]
12. Krokan HE & Bjoras M Base excision repair. Cold Spring Harb Perspect Biol 5, a012583, doi:10.1101/cshperspect.a012583 (2013). [PubMed: 23545420]
13. Strumberg D et al. Conversion of topoisomerase I cleavage complexes on the leading strand of ribosomal DNA into 5’-phosphorylated DNA double-strand breaks by replication runoff. Mol Cell Biol 20, 3977–3987, doi:10.1128/mcb.20.11.3977-3987.2000 (2000). [PubMed: 10805740]
14. Yu K & Lieber MR Current insights into the mechanism of mammalian immunoglobulin class switch recombination. Crit Rev Biochem Mol Biol 54, 333–351, doi:10.1080/10409238.2019.1659227 (2019). [PubMed: 31509023]
15. Cortes-Ciriano I et al. Comprehensive analysis of chromothripsis in 2,658 human cancers using whole-genome sequencing. Nat Genet, doi:10.1038/s41588-020-0634-1 (2020).
16. Shoshani O et al. Chromothripsis drives the evolution of gene amplification in cancer. Nature 591, 137–141, doi:10.1038/s41586-020-03064-z (2021). [PubMed: 33361815]
17. Kloosterman WP & Cuppen E Chromothripsis in congenital disorders and cancer: similarities and differences. Curr Opin Cell Biol 25, 341–348, doi:10.1016/j.ceb.2013.02.008 (2013). [PubMed: 23478216]
18. Tan EH et al. Catastrophic chromosomal restructuring during genome elimination in plants. Elife 4, doi:10.7554/eLife.06516 (2015).
19. Carvalho CM & Lupski JR Mechanisms underlying structural variant formation in genomic disorders. Nat Rev Genet 17, 224–238, doi:10.1038/nrg.2015.25 (2016). [PubMed: 26924765]
20. Crasta K et al. DNA breaks and chromosome pulverization from errors in mitosis. Nature 482, 53–58, doi:10.1038/nature10802 (2012). [PubMed: 22258507]
21. Lemmens B et al. DNA Replication Determines Timing of Mitosis by Restricting CDK1 and PLK1 Activation. Mol Cell 71, 117–128 e113, doi:10.1016/j.molcel.2018.05.026 (2018). [PubMed: 30008317]
22. Masuda Y, Bennett RA & Demple B Dynamics of the interaction of human apurinic endonuclease (Ape1) with its substrate and product. J Biol Chem 273, 30352–30359, doi:10.1074/jbc.273.46.30352 (1998). [PubMed: 9804798]
23. Lau AY, Wyatt MD, Glassner BJ, Samson LD & Ellenberger T Molecular basis for discriminating between normal and damaged bases by the human alkyladenine glycosylase, AAG. Proc Natl Acad Sci U S A 97, 13573–13578, doi:10.1073/pnas.97.25.13573 (2000). [PubMed: 11106395]
24. Shimizu N, Kanda T & Wahl GM Selective capture of acentric fragments by micronuclei provides a rapid method for purifying extrachromosomally amplified DNA. Nat Genet 12, 65–71, doi:10.1038/ng0196-65 (1996). [PubMed: 8528254]
25. Pang B et al. Defects in purine nucleotide metabolism lead to substantial incorporation of xanthine and hypoxanthine into DNA and RNA. Proc Natl Acad Sci U S A 109, 2319–2324, doi:10.1073/pnas.1118455109 (2012). [PubMed: 22308425]
26. Sakumi K et al. ITPA protein, an enzyme that eliminates deaminated purine nucleoside triphosphates in cells. Mutat Res 703, 43–50, doi:10.1016/j.mrgentox.2010.06.009 (2010). [PubMed: 20601097]

27. Gaudelli NM et al. Programmable base editing of A*T to G*C in genomic DNA without DNA cleavage. Nature 551, 464–471, doi:10.1038/nature24644 (2017). [PubMed: 29160308]
28. Zheng Y, Lorenzo C & Beal PA DNA editing in DNA/RNA hybrids by adenosine deaminases that act on RNA. Nucleic Acids Res 45, 3369–3377, doi:10.1093/nar/gkx050 (2017). [PubMed: 28132026]
29. Shiromoto Y, Sakurai M, Minakuchi M, Ariyoshi K & Nishikura K ADAR1 RNA editing enzyme regulates R-loop formation and genome stability at telomeres in cancer cells. Nat Commun 12, 1654, doi:10.1038/s41467-021-21921-x (2021). [PubMed: 33712600]
30. Jimeno S et al. ADAR-mediated RNA editing of DNA:RNA hybrids is required for DNA double strand break repair. Nat Commun 12, 5512, doi:10.1038/s41467-021-25790-2 (2021). [PubMed: 34535666]
31. Crossley MP, Bocek M & Cimprich KA R-Loops as Cellular Regulators and Genomic Threats. Mol Cell 73, 398–411, doi:10.1016/j.molcel.2019.01.024 (2019). [PubMed: 30735654]
32. Smolka JA, Sanz LA, Hartono SR & Chedin F Recognition of RNA by the S9.6 antibody creates pervasive artifacts when imaging RNA:DNA hybrids. J Cell Biol 220, doi:10.1083/jcb.202004079 (2021).
33. Makharashvili N et al. Sae2/CtIP prevents R-loop accumulation in eukaryotic cells. Elife 7, doi:10.7554/eLife.42733 (2018).
34. Chen L et al. R-ChIP Using Inactive RNase H Reveals Dynamic Coupling of R-loops with Transcriptional Pausing at Gene Promoters. Mol Cell 68, 745–757 e745, doi:10.1016/j.molcel.2017.10.008 (2017). [PubMed: 29104020]
35. Nishikura K A-to-I editing of coding and non-coding RNAs by ADARs. Nat Rev Mol Cell Biol 17, 83–96, doi:10.1038/nrm.2015.4 (2016). [PubMed: 26648264]
36. Liu Y et al. RNA abasic sites in yeast and human cells. Proc Natl Acad Sci U S A 117, 20689–20695, doi:10.1073/pnas.2011511117 (2020). [PubMed: 32788345]
37. Han L et al. The Genomic Landscape and Clinical Relevance of A-to-I RNA Editing in Human Cancers. Cancer Cell 28, 515–528, doi:10.1016/j.ccell.2015.08.013 (2015). [PubMed: 26439496]
38. Tsuruoka N et al. ADAR1 protein induces adenosine-targeted DNA mutations in senescent Bcl6 gene-deficient cells. J Biol Chem 288, 826–836, doi:10.1074/jbc.M112.365718 (2013). [PubMed: 23209284]
39. Li JB et al. Genome-wide identification of human RNA editing sites by parallel DNA capturing and sequencing. Science 324, 1210–1213, doi:10.1126/science.1170995 (2009). [PubMed: 19478186]
40. Eggington JM, Greene T & Bass BL Predicting sites of ADAR editing in double-stranded RNA. Nat Commun 2, 319, doi:10.1038/ncomms1324 (2011). [PubMed: 21587236]
41. Alexandrov LB et al. The repertoire of mutational signatures in human cancer. Nature 578, 94–101, doi:10.1038/s41586-020-1943-3 (2020). [PubMed: 32025018]
42. Maciejowski J et al. APOBEC3-dependent kataegis and TREX1-driven chromothripsis during telomere crisis. Nat Genet 52, 884–890, doi:10.1038/s41588-020-0667-5 (2020). [PubMed: 32719516]
43. Mohr L et al. ER-directed TREX1 limits cGAS activation at micronuclei. Mol Cell 81, 724–738 e729, doi:10.1016/j.molcel.2020.12.037 (2021). [PubMed: 33476576]
44. Vietri M et al. Unrestrained ESCRT-III drives micronuclear catastrophe and chromosome fragmentation. Nat Cell Biol 22, 856–867, doi:10.1038/s41556-020-0537-5 (2020). [PubMed: 32601372]
45. Maass KK et al. Altered nuclear envelope structure and proteasome function of micronuclei. Exp Cell Res 371, 353–363, doi:10.1016/j.yexcr.2018.08.029 (2018). [PubMed: 30149001]
46. Ruzov A et al. Lineage-specific distribution of high levels of genomic 5-hydroxymethylcytosine in mammalian development. Cell Res 21, 1332–1342, doi:10.1038/cr.2011.113 (2011). [PubMed: 21747414]
47. Taghizadeh K et al. Quantification of DNA damage products resulting from deamination, oxidation and reaction with products of lipid peroxidation by liquid chromatography isotope dilution tandem mass spectrometry. Nat Protoc 3, 1287–1298, doi:10.1038/nprot.2008.119 (2008). [PubMed: 18714297]

48. Yu Y et al. Comprehensive Assessment of Oxidatively Induced Modifications of DNA in a Rat Model of Human Wilson's Disease. Mol Cell Proteomics 15, 810–817, doi:10.1074/mcp.M115.052696 (2016). [PubMed: 26362317]

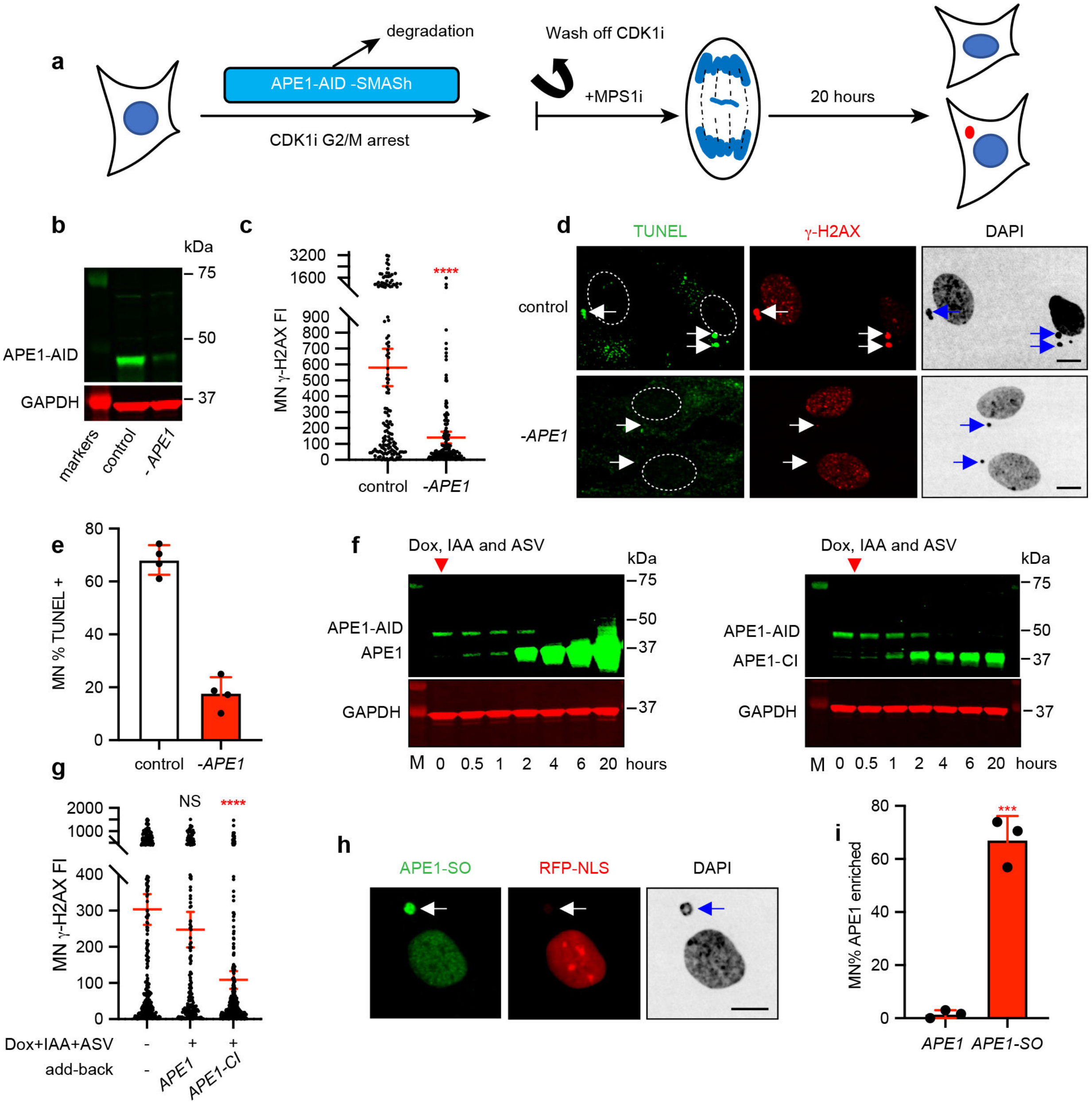

Figure 1. The APE1 endonuclease is required for DNA damage in micronuclei.

(**a**) Scheme of the procedure for cell synchronization and the induction of micronuclei. For RNAi treatments, siRNAs were transfected 24 hours prior to synchronization. For conditional protein degradation, doxycycline (dox), synthetic auxin IAA (3-indoleacetic acid), and asunaprevir (ASV) were added with RO-3306 (CDK1i). MPS1i is NMS-P715. (**b**) Representative western blot showing APE1-AID-SMASh degradation. Note that prior to drug addition, the SMASh tag is auto-cleaved, leaving the APE1-AID fusion. Control: no drugs; -APE1: 1 hour drug treatment (Dox, IAA and ASV). GAPDH is the loading control. (**c**) MN **γ**-H2AX fluorescence intensity (FI, arbitrary units) with or without APE1 degradation (mean with 95% CI, ****P<0.0001, Two-tailed Mann-Whitney U test, control: n=145; -APE: n=150).

(**d**) Representative images of cells with or without APE1 depletion. TUNEL assay: green; γ-H2AX: red; white and blue arrows: MN. Dotted white lines outline the PN. Unless otherwise indicated, all scale bars in this study: 10 μm unless specified.

(**e**) % TUNEL positive MN with or without APE1 depletion (mean with SD, ****$P<0.0001$, two-tailed unpaired t-test, 4 independent experiments, control: n=506, -APE1: n=540). % positive, here, and throughout the paper is >3 SD above the background subtracted primary nucleus signal.

(**f**) Western blot showing induced-expression of APE1 or APE1-CI (catalytic inactive variant, H309N) after APE1-AID-SMASh degradation. Note: although APE1-CI is expressed at lower levels than exogenous APE1, its steady state levels are higher than endogenous APE1. GAPDH is the loading control. M, molecular markers.

(**g**) MN γ-H2AX FI for the indicated samples (mean with 95% CI, add-back samples were compared with the no degradation control. NS, $P=0.1046$, ****$P<0.0001$, Ordinary one-way ANOVA with Dunnett’s multiple comparisons test. control: n=288; *APE1-WT* add-back: n=177; *APE1-CI* add-back: n=280).

(**h**) Representative immunofluorescence image of another catalytic inactive APE1 variant (APE1-SO: D283A, D308A). Add-back and induction as in Fig. 1f. NE rupture detected by the loss of RFP-NLS. White and blue arrows: MN.

(**i**) % MN with accumulation of APE1-SO as in (h) above, (mean with SD, ***$P=0.0002$, two-tailed unpaired t-test, 3 experiments, control: n= 121; *APE1-SO*: n=198).

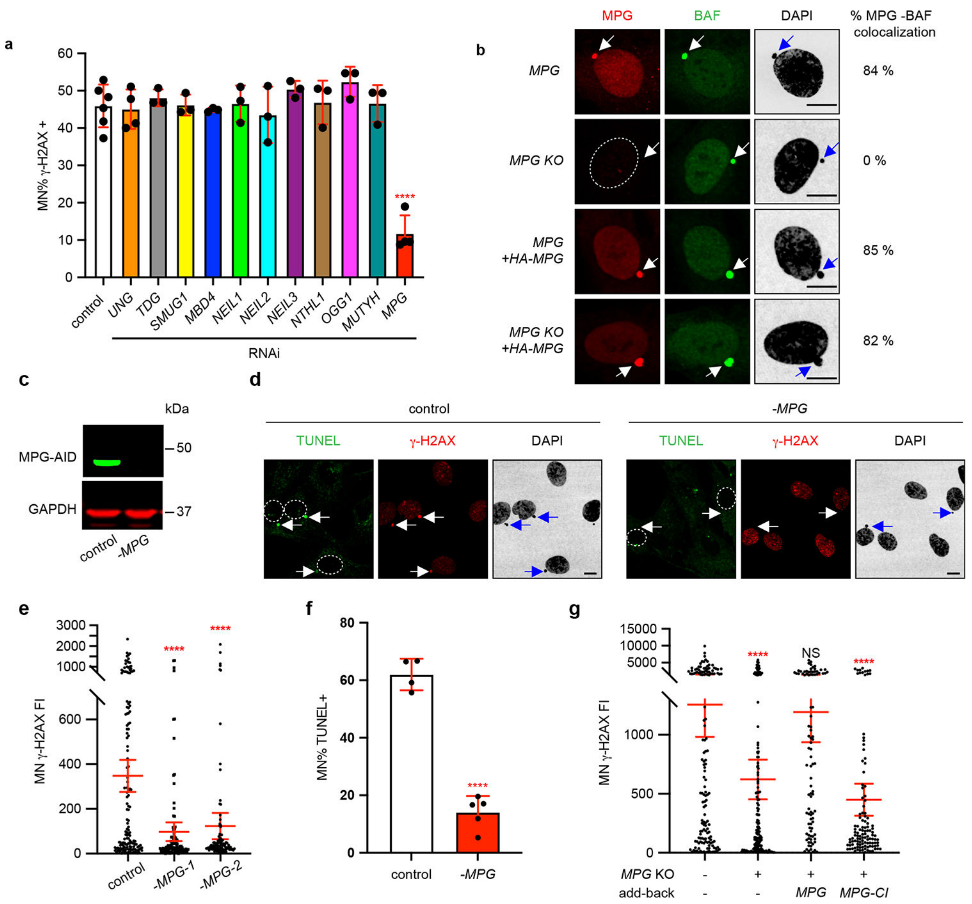

Figure 2. MPG is required for DNA damage in micronuclei.

(**a**) RNAi screen of the 11 DNA glycosylases for their requirement in generating MN DNA damage. RPE-1 cells were synchronized as in Fig. 1a. (mean with SD; ****P<0.0001, Ordinary one-way ANOVA with Dunnett's multiple comparisons test; >3 independent experiments for each RNAi treatment. N values from left to right: n=658, 377, 276, 305, 303, 302, 288, 346, 318, 322, 291, 460. P values for each sample left to right compared to the control: 0.9997, 0.9968, >0.9999, 0.9996, 0.9998, 0.9960, 0.8283, 0.9997, 0.4312, 0.9998, and <0.0001).

(**b**) MPG accumulates on ruptured MN. Genotype is indicated on the left. HA-tagged MPG is expressed from the CMV promoter. % MN visibly positive for MPG are shown on the right. BAF accumulation was used as a marker for ruptured MN. Dotted white lines outline the PN. White and blue arrows: MN.

(**c**) Western blot to detect MPG-AID-SMASh in RPE-1 cells synchronized as in Fig. 1a. Control: no drugs; -MPG: dox, IAA, ASV. GAPDH is the loading control.

(**d**) Representative images of cells with or without MPG degradation. Two different DNA damage markers are used: TUNEL assay: green; γ-H2AX: red; white and blue arrows: MN. Dotted white lines outline the PN.

(**e**) Degradation of MPG suppresses DNA damage in MN. MN γ-H2AX FI measurements for the experiment in Fig. 2c above. Shown is data from two independent MPG-AID-SMASh RPE-1 lines (mean with 95% CI, two MPG-AID-SMASh clones were compared to the no degradation control. ****$P<0.0001$, Ordinary one-way ANOVA with Dunnett's multiple comparisons test. control: n=149; -MPG-1: n=112; -MPG-2: n=110).

(**f**) Aggregated data from four replicates scoring % TUNEL positive MN, before and after MPG degradation as in Fig. 2c above (mean with SD, ****$P<0.0001$, two-tailed unpaired t-test, control: n=593, -MPG: n=544).

(**g**) The catalytic activity of MPG is required for MN DNA damage. MN γ-H2AX FI measurements were made in the indicated cell lines and conditions. MPG catalytic inactive variant, *MPG-CI*, is *MPG-E215A* (mean, 95% CI, *MPG* KO with add-back constructs were compared to an *MPG* control. NS: P=0.9658; ****P<0.0001, Ordinary one-way ANOVA with Dunnett's Multiple comparisons test. control: n=153; *MPG* KO: n=169; *MPG* add-back: n=96; *MPG-CI* add-back: n=117).

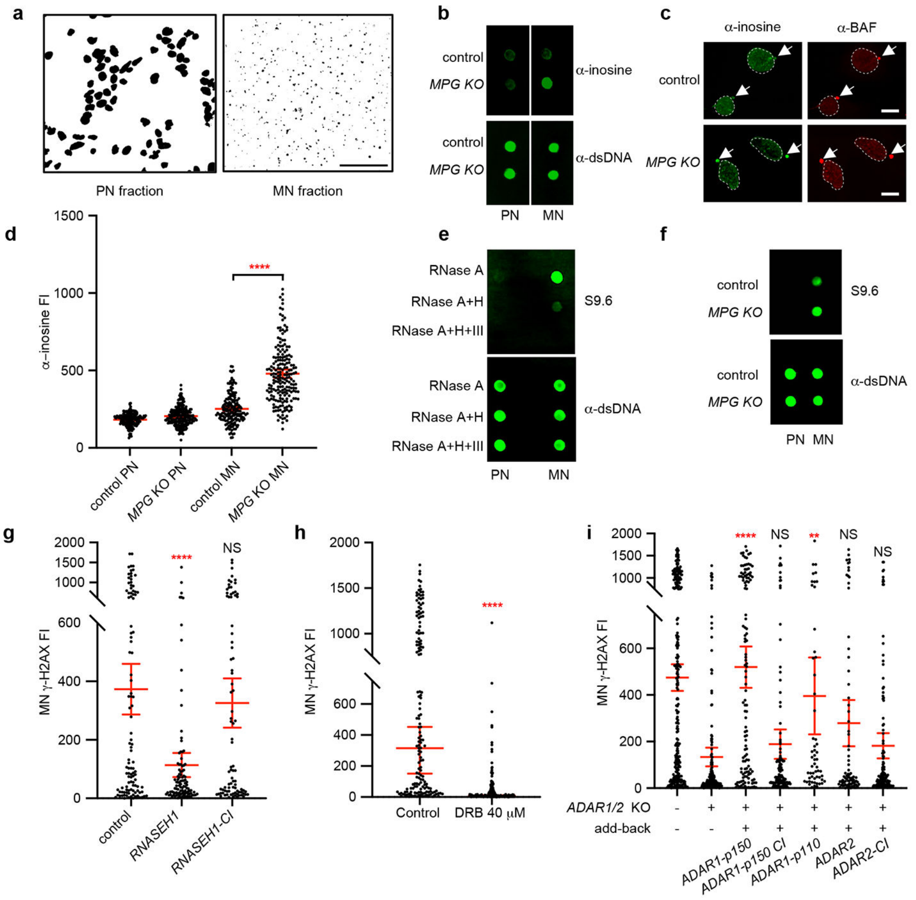

Figure 3. ADAR-mediated deamination of RNA-DNA hybrids promotes MN DNA damage.

(**a**) Inverted contrast images of DAPI-stained PN and MN isolated by sequential sucrose gradients from U2OS cells. Scale bar: 50 μm.

(**b**) Dot blot to detect I and/or dI from purified PN and MN in control and *MPG* KO cells. α-dsDNA is the loading control.

(**c**) Images of α-inosine immunostaining in ruptured MN from wild type and *MPG* KO cells. BAF accumulation marks MN rupture. White arrows: MN. Dotted white lines outline the PN.

(**d**) α-inosine FI in control and *MPG* KO cells as shown in Fig. 3c (mean with 95% CI, *****P*<0.0001, Ordinary one-way ANOVA with Tukey's multiple comparisons test. control: n=173; *MPG* KO: n=201).

(**e**) Dot blot to detect RNA-DNA hybrids with S9.6 from purified PN and MN with different RNase treatments. α-dsDNA is the loading control.

(**f**) Dot blot showing the S9.6 FI in purified PN and MN from wild-type and *MPG* KO U2OS cells. α-dsDNA is the loading control.

(**g**) Overexpression of RNaseH1 suppresses DNA damage in MN. MN γ-H2AX FI measured in controls or cells overexpressing either wild-type RNaseH1 or catalytically inactive (RNaseH1-CI, D210N) cells. Induced expression of RNaseH1 or RNaseH1-CI is from a Tet-on promoter. Dox was added during the G2/M arrest as shown in Fig. 1a (mean with 95% CI, RNaseH1 and RNaseH1-CI were compared to the no dox control. NS, *P*=0.5763, ****$P<0.0001$, Ordinary one-way ANOVA with Dunnett's multiple comparisons test. control: 108; *RNASEH1*: n=106; *RNASEH1-CI*: n=88).

(**h**) MN γ-H2AX fluorescence intensity in EdU positive cells with or without 40 μM DRB (mean with 95% CI, ****$P<0.0001$, Two-tailed Mann-Whitney U test, control: n=162; DRB: n=170).

(**i**) ADAR1 and ADAR2 independently contribute to DNA damage in MN. MN γ-H2AX FI measured in the indicated cell lines with the indicated add-back constructs (mean with 95% CI, The indicated add-back samples are compared to the control on the far left. NS, *P*=0.9348 for *ADAR1-p150-CI* add-back, NS, *P*=0.1555 for the *ADAR2* add-back, NS, *P*=0.9634 for the *ADAR2-CI* add-back, ****$P<0.0001$, ***P*=0.001 Ordinary one-way ANOVA with Tukey's multiple comparisons test. N values from left to the right: n=264, 162, 129, 118, 59, 81, 123). Statistical analysis showing that the rescue of the *ADAR1/2* knockout by ADAR2 add-back is significant is shown in Extended Data Fig. 10c.

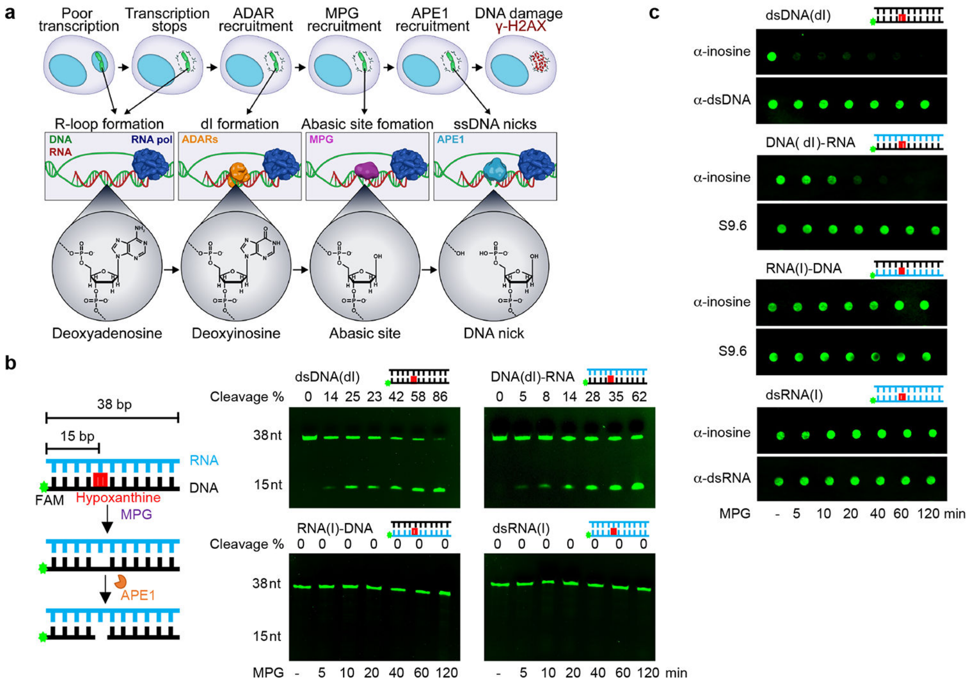

Figure 4. MPG can remove deoxyinosine from the DNA strand of RNA:DNA hybrids.

(**a**) Model summarizing the results of this study. Top panel from left to the right: the cellular events leading to MN DNA damage during interphase. The reason MN accumulate RNA:DNA hybrids is not known but could occur before and/or after NE ruptures. Middle panel: molecular events in MN in the top panel. Bottom panel: zoomed images with the indicated chemical structures.

(**b**) **Left**. Scheme of the experiment. **Right**. MPG removes dI from RNA:DNA hybrids. Urea-PAGE gel images to detect specific cleavage at I or dI residues on the labeled strand. Variable times of MPG incubation are indicated, all followed by 5 minutes APE1 digestion. Cleavage efficiency is the FI of the cleavage product divided by the total FI signal in the lane. % cleavage values are averaged from three replicates.

(**c**) Images of a-inosine dot blots showing digested products of indicated substrates by MPG for indicated amount of time.